Rahaman, W., Wittmann, H., von Blanckenburg, F. (2017): Denudation rates and the degree of chemical weathering in the Ganga River basin from ratios of meteoric cosmogenic 10Be to stable 9Be. - *Earth and Planetary Science Letters*, *469*, pp. 156—169.

DOI: http://doi.org/10.1016/j.epsl.2017.04.001

Denudation rates and the degree of chemical weathering in the Ganga River basin from ratios of meteoric cosmogenic ^{10}Be to stable ^{9}Be

Accepted version, April 2017

Waliur Rahaman[1, 2], Hella Wittmann[1] & Friedhelm von Blanckenburg[1,3]

[1]GFZ German Research Centre for Geosciences, Potsdam, Germany

[2]ESSO-National Centre for Antarctic & Ocean Research, Goa, India

[3]Institute of Geological Sciences, Freie Universität Berlin, Germany

Keywords:

Meteoric cosmogenic ^{10}Be

Denudation

Chemical weathering

Himalaya

Ganga

Abstract

The ratio of the meteoric cosmogenic nuclide ^{10}Be, precipitated from the atmosphere, to the stable nuclide ^{9}Be, released by silicate weathering, was measured in suspended sediment of the Ganga River basin to determine denudation rates, degrees of weathering, and sediment storage in the floodplain. The ^{10}Be precipitated and the ^{9}Be released are carried to ca. 90% by amorphous and to 10% by crystalline Fe-hydroxides, as revealed by chemical extractions, whereas the dissolved Be transport is negligible due to the river pH of 8. Resulting $^{10}Be/^{9}Be$ ratios increase from 0.75×10^{-9} for the northern and Himalaya-draining rivers to 1.7×10^{-9} in the downstream basin. The increase in $^{10}Be/^{9}Be$ ratios results from two compounding effects: 1) average denudation rates decrease from 0.5 mm yr^{-1} in the Himalayas to 0.17 mm yr^{-1} for the Ganga main stem in the lowlands, 2) the southern tributaries draining the low-relief craton contribute sediment with a ratio of 2.0×10^{-9}, corresponding to a denudation rate of 0.03 mm yr^{-1}. We find that at the spatial scale of the entire basin, the atmospheric delivery flux of ^{10}Be equals its sedimentary export flux. Hence fluxes can be considered to be at steady state and radioactive decay of ^{10}Be during sediment storage is not discernible. The lack of a resolvable increase in ^{10}Be concentration during sediment transfer along the floodplain stretch furthermore suggests that sediment transfer time is indeed short. We also cannot resolve any additional release of silicate-bound ^{9}Be in the floodplain, testifying to the low degree of weathering there. When multiplied with the basin area the $^{10}Be/^{9}Be$-derived denudation rate of 0.14 mm yr^{-1} at the most downstream location corresponds to a sediment flux of 350 Mt yr^{-1} which is in good agreement with gauging-derived sediment fluxes (ca. 400 Mt yr^{-1}). Because they integrate over the entire basin, denudation rates from $^{10}Be/^{9}Be$ are lower than floodplain-corrected denudation rates from *in situ* cosmogenic ^{10}Be that reflect the rates of the sediment-producing mountain areas.

1. Introduction

Large amounts of sediments are mobilized from the Himalayan headwaters and transferred downstream through the Ganga plain to be finally deposited in the Bengal submarine fan (Galy et al., 2007; Rahaman et al., 2009). Several methods have been employed to estimate denudation rates and degree of weathering in the Himalayan headwaters and in the Ganga plain, ranging from present-day sediment budgets and gauging (Gabet et al., 2008; Galy and France-Lanord, 2001; Lupker et al., 2011) to millennial-scale *in situ* cosmogenic ^{10}Be (Lupker et al., 2012a; Scherler et al., 2014; Vance et al., 2003), long-term thermochronology based on cooling ages (Burbank et al., 2003; Herman et al., 2010; Thiede et al., 2009), river incision rates (Lavé and Avouac, 2001), and geochemical proxies (Bagard et al., 2015; France-Lanord et al., 1993; Frings et al., 2015; Kısakűrek et al., 2005; Lupker et al., 2011; Rahaman et al., 2011). With such density of published data, the Ganga plain and its headwaters constitute a natural laboratory where novel methods to quantify riverine sediment fluxes can be tested.

Using the cosmogenic radioactive ($t_{1/2}$ = 1.39 Myr) meteoric isotope ^{10}Be and the stable isotope ^{9}Be, we present denudation, erosion, and index of weathering for the Ganga basin. Meteoric ^{10}Be is produced in the atmosphere by spallation reactions that we use as an atmospheric deposition tracer while ^{9}Be is released from weathering of rocks (von Blanckenburg et al., 2012). In rivers, ^{10}Be/^{9}Be ratios that can be measured in both water and authigenic fractions extracted from bedload or suspended sediment have great potential for quantifying denudation, erosion and degree of weathering on the large sub-continental scale (von Blanckenburg et al., 2012; Wittmann et al., 2015).

Here we use the new $^{10}Be/^{9}Be$ system to provide kyr time scale sediment fluxes and extents of chemical weathering intensities. We compare these fluxes to those from other methods, mainly those from *in situ* cosmogenic ^{10}Be, as integration time scales for both methods are thought to be similar (Willenbring & von Blanckenburg, 2010; Foster et al., 2015). We test whether *in situ* cosmogenic nuclides and $^{10}Be/^{9}Be$ ratios are modified during floodplain transfer and storage. We show that the steady-state of meteoric ^{10}Be with respect to input from atmospheric deposition and its export by riverine transfer has been established in the Ganga floodplain, and we show that sediment storage in the floodplain is too short to result in resolvable release of silicate-bound ^{9}Be by weathering in the floodplain.

1.1 Summary of the conceptual framework for simultaneously deriving E, D and the degree of weathering ($f_{reac}+f_{diss}$)

We summarize the conceptual framework developed by von Blanckenburg et al. (2012) , and present the relevant equations that will be used in this paper. In order to maintain consistency for the terminologies and notations used here, we adopt those of Wittmann et al. (2015). The ^{9}Be contained in bedrock, defined as $^{9}Be_{parent}$, continuously enters the critical zone during advance of the weathering front and during weathering of primary minerals in the regolith (Maher and von Blanckenburg, 2016). Partial dissolution of bedrock and minerals leads to release of ^{9}Be, called mobilized fraction, and a fraction of ^{9}Be that remains locked in primary minerals, $^{9}Be_{min}$. Due to its particle-reactive nature, the mobilized ^{9}Be that is released during weathering readily adsorbs onto mineral surfaces or co-precipitates with Fe-Al-(hydr-) oxides, or clays, collectively called $^{9}Be_{reac}$. The ^{9}Be remaining in solution, termed $^{9}Be_{diss}$, is exported in the dissolved form. These different ^{9}Be pools can be accessed

via sequential chemical extraction (Wittmann et al. 2012). Meteoric ^{10}Be is delivered into the top of the weathering zone via wet and dry deposition (Willenbring and von Blanckenburg, 2010). Similar to ^{9}Be, dissolved ^{10}Be adsorbs onto mineral surfaces (von Blanckenburg et al., 2012). The partitioning between dissolved and reactive Be is highly pH-dependent, where the solid-fluid partition coefficient K_d is 10^3 at pH of 4 and 10^5 to 10^6 at circumneutral pH (Maher and von Blanckenburg, 2016). As pH values exceed 8 (Table 1) in Ganga soil solutions and river water, the dissolved fractions of both ^{9}Be and ^{10}Be are negligible relative to the reactive pool. If we ignore radioactive decay of ^{10}Be during fast erosion, an erosion rate E_{met} can be calculated from the simplified equations of von Blanckenburg et al. (2012):

$$E_{met} = \frac{F_{met}^{10Be}}{[^{10}Be]_{reac}} \quad (1)$$

where E_{met} is the erosion rate (in kg m^{-2} yr^{-1}), F_{met}^{10Be} is the depositional flux of meteoric ^{10}Be to the Earth's surface (in at m^{-2} yr^{-1}), and $[^{10}Be]_{reac}$ is the reactive ^{10}Be concentration as determined by chemical extractions (in at kg$_{solid}^{-1}$). By combining the isotope mass balances for ^{9}Be and ^{10}Be, assuming equilibration between dissolved and reactive ^{10}Be/^{9}Be, and ignoring negligible (compared to analytical uncertainty) mass-dependent isotope fractionation, a denudation rate D_{met} can be calculated from the simplified equation of von Blanckenburg et al. (2012):

$$D_{met} = \frac{F_{met}^{10Be}}{\left(\frac{^{10}Be}{^{9}Be}\right)_{reac} \times [^{9}Be]_{parent} \times (f_{reac}^{9Be} + f_{diss}^{9Be})} \quad (2)$$

where the D_{met} is the denudation rate (in kg m^{-2} yr^{-1}), which can be converted to mass flux per time (t yr^{-1}) by multiplying with area, or to length per time (mm yr^{-1}) by dividing by a bedrock density of 2600 kg m^{-3}. $(^{10}Be/^{9}Be)_{reac}$ is the ratio of ^{10}Be and ^{9}Be in chemically extracted Be; $[^{9}Be]_{parent}$ is the concentration of ^{9}Be in the unweathered bedrock (in kg kg_{rock}^{-1}), and the term $f_{reac}^{9Be} + f_{diss}^{9Be}$ presents the mobilized flux fraction of ^{9}Be that is released from primary minerals during weathering. The mobilized flux fraction of ^{9}Be can be estimated by two separate approaches (Wittmann et al., 2015), one entailing the concentrations of $[^{9}Be]_{reac}$ and $[^{9}Be]_{min}$ (eq. 3), and one using the river´s sedimentary and dissolved fluxes. In absence of significant dissolved ^{9}Be contributions however, the latter approach yields the same results as the approach using concentrations measured on river sediment :

$$\mathrm{f_{reac}^{9Be} + f_{diss}^{9Be} = \frac{[\,^{9}Be]_{reac}}{([\,^{9}Be]_{reac} + [\,^{9}Be]_{min})}} \quad (3)$$

A requirement for using the framework presented above is that the inputs of ^{10}Be into a drainage basin, derived from knowing the depositional flux, balance the outputs of ^{10}Be, by export from riverine and dissolved fluxes. The basin-wide atmospheric input of ^{10}Be, $\mathrm{J_{atm}^{10Be}}$, at yr^{-1}, reaching the total basin´s surface area, $A_{riv,i}$, in m^{-2}, with n = i being all summed subbasins, is given by :

$$\mathrm{J_{atm}^{10Be}} = \sum_{i=1}^{n} \mathrm{A_{riv,i} \times F_{met,i}^{10Be}} \quad (4)$$

The total meteoric flux of ^{10}Be exported by the river system, $J_{riv}^{^{10}Be}$, in at yr^{-1}, is given by:

$$J_{riv}^{^{10}Be} = J_{riv\_reac}^{^{10}Be} + J_{riv\_diss}^{^{10}Be} = \sum_{i=1}^{n} \left[\left(A_{riv,i} \times E_i \times \left[^{10}Be \right]_{reac,i} + Q_i \times \left[^{10}Be \right]_{diss,i} \right) \times \left(1 - \exp^{(-\lambda t(i))} \right) \right] \quad (5)$$

where $J_{riv\_reac}^{^{10}Be}$ and $J_{riv\_diss}^{^{10}Be}$ are the sum of the riverine fluxes of ^{10}Be in the reactive (adsorbed and secondary solids) and dissolved fractions (in at yr^{-1}), respectively. The $J_{riv\_reac}^{^{10}Be}$ and $J_{riv\_diss}^{^{10}Be}$ terms can be calculated as the product of areas for all subbasins i, $A_{riv,i}$, an independently-derived long-term erosion rate, E, in kg m^{-2} yr^{-} (i.e. from *in situ* ^{10}Be), and ^{10}Be concentrations in the reactive fraction ($[^{10}Be]_{reac,i}$, in at kg$_{solid}^{-1}$), in addition to the product of river discharge Q_i and dissolved ^{10}Be concentrations, $[^{10}Be]_{diss,i}$ (in at L_{water}^{-1}), respectively. In absence of significant dissolved ^{10}Be contribution, however, $J_{riv}^{^{10}Be}$ is mainly composed of $J_{riv\_reac}^{^{10}Be}$. The right-hand term in equation 5 describes the basin-averaged radioactive decay of ^{10}Be during sediment transfer and storage with the decay constant λ (5×10^{-7} yr^{-1}) corresponding to a half-life of 1.39 Myr (Chmeleff et al., 2010; Korschinek et al., 2010) and t(i) is the sediment storage time in each subbasin. The balance of ^{10}Be fluxes is attained if $J_{riv}^{^{10}Be} = J_{atm}^{^{10}Be}$.

2 Study area and sampling

The Ganga basin at Farakka covers an area of about 10^6 km^2, comprising three major physiographic units which are the Himalayas in the north, the Vindhyan super groups and the Bundelkhand Plateau of peninsular India in the south, and the Ganga plain between them (Fig. 1A). Among the major tributaries, the Yamuna, Ghagra, Gandak and the Kosi join the Ganga from north, whereas the Yamuna on its way south collects the southern tributaries draining peninsular India, such as the Chambal River, before its confluence with the Ganga (Fig. 1). Lithologies in the headwaters of the Ganga basin range from Archean granites in the Indian craton to carbonate and quartz-bearing metasedimentary rocks of the Higher Himalayas (see Fig. 1A). The Ganga plain is mainly comprised of unconsolidated Quaternary alluvium. Basin's surface areas, discharge, and pH of river water measured during sampling, are provided in Table 1. The pH measurements were conducted at point locations during sampling and are consistent with earlier reported values of pH time series (Sarin et al., 1989; Rai et al., 2010). The annual sediment flux of the Ganga, derived from suspended sediment measurements, amounts to 500-600 Mt yr^{-1} (Galy and France-Lanord, 2001; Lupker et al., 2011). Floodplain-corrected denudation rates derived from *in situ* cosmogenic ^{10}Be record the Himalayan headwater erosion over integration time scales of ca. 10^3 yr and amount to ca. 0.8 to 1 mm yr^{-1} (where "floodplain correction" means that production rates have been adjusted to exclude those lowland areas that do not produce any fresh sediment, cf. Wittmann et al. (2011)). These rates can be converted into a sediment flux of ca. 700 Mt yr^{-1} in the Ganga lowlands (Lupker et al., 2012a).

Suspended sediment samples were collected during peak discharge from the Ganga main stem and its principal tributaries from Rishikesh (Ganga headwaters) to the final outflow in the plain at Manikchak (Fig. 1). At each location, about 1 liter of river water was collected, pH values were recorded (ranging from values of 8 to 8.8, Table 1) and then filtered on-site using 0.22 µm porosity cellulose acetate filters. After filtration, filters were brought to the laboratory and dried at 50 °C. Dried suspended material was then recovered from the filter papers for analysis.

3 Methods

3.1 Grain size analysis of suspended sediments

Oven-dried sample aliquots were treated with 10% H_2O_2 and 10% HCl to remove organic and calcium-carbonate compounds. The samples were dispersed with sodium pyrophosphate for 24 h and placed in an ultrasonic bath for 15 min prior to measurement. Grain-size distributions were measured using laser diffraction particle sizer at GFZ Potsdam (Model Retsch-Horiba LA-950), providing 92 classes between 0.01 and 2500 µm. Prior to each measurement, the sample was exposed to 10 s ultrasonic excitation to mechanically disaggregate particles. The median distribution of 10 consecutive measurements per sample was used for further statistical analysis. Statistical analysis was performed using the excel-based GRADISTAT software (Blott and Pye, 2001) to obtain clay (<2 µm) abundance (%) and the D_{84} (in µm) which denotes the grain size at which 84% of the sample is smaller. The results of these analyses are presented in Table 1.

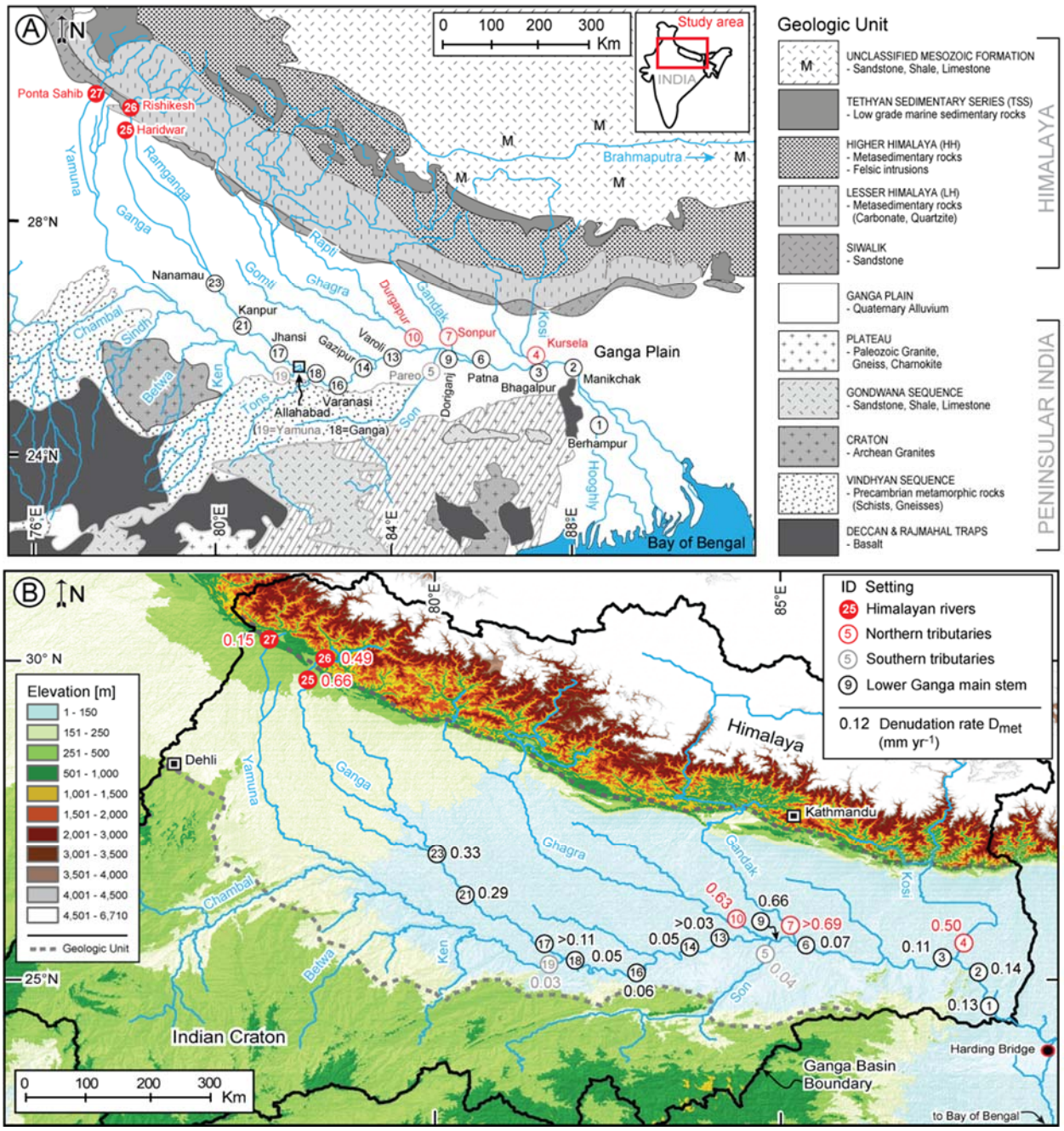

Figure 1) A: Lithological map of the Ganga basin, modified after Sarin et al. (1989), colored circles indicate sampling IDs. B: SRTM-derived elevation map of the Ganga basin with detailed drainage network. Stippled grey lines separate geological units, i.e. Himalayas, Indian Craton, and Ganga lowlands. Numbers next to sampling IDs denote denudation rates D_{met}* (mm yr^{-1}) (for explanation, see Section 6).

Table 1: Basin and sample characteristics

Sample ID	River	Location	Latitude (°N)	Longitude (°E)	pH during sampling	Sampling altitude (m)	Distance from source (km)	Grain size parameters[a]		Total drainage area (x10^3 km^2)	Water discharge (x10^9 m^3 yr^{-1})[b]	FC-Denudation rate from *in situ* ^{10}Be (mm yr^{-1})[c]	FC-Sediment flux from *in situ* ^{10}Be (Mt yr^{-1})[d]	Sediment flux Q_M from river load gauging (Mt yr^{-1})[e]
								D_{84} (µm)	Clay-sized fraction (%)					
Distributary of the Ganga														
GMSS-1	Ganga	Berhampur	24.1000	88.2450	8.2	19	2043	52	6.44	3.3		0.92 ± 0.17	524 ± 99	
Ganga Main stream														
GMSS-2	Ganga	Manikchak	25.0630	87.8781	8.2	40	1895	12	10.5	935	380	0.92 ± 0.17	524 ± 99	390
GMSS-3	Ganga	Bhagalpur	25.2869	87.0269	8.1	37	1756	48	10.3	830		0.92 ± 0.17	524 ± 99	390
GMSS-6	Ganga	Patna	25.6214	85.2069	8.1	56	1529	38	13.9	776	240.5	0.63 ± 0.15	253 ± 59	130
GMSS-9	Ganga	Doriganj	25.7299	84.8304	8.2	56	1485	42	4.05	663				
GMSS-13	Ganga	Varoli	25.5911	83.9853	8.2	53	1378	92	13.8	518				
GMSS-14	Ganga	Gazipur	25.5863	83.6056	8.3	57	1331	96	13.4	507				
GMSS-16	Ganga	Varanasi	25.3205	83.0370	8.1	75	1225	46	13.8	468	130.5	0.398 ± 0.084	47.10 ± 9.90	
GMSS-17	Ganga	Jhansi	25.4429	81.9020	8.0	80	1017	-	-	92.3				
GMSS-18	Ganga	Allhabad	25.4023	81.8973	8.1	89	1022	11	20.8	446	59.0			
GMSS-21	Ganga	Kanpur	26.4375	80.4107	8.2	113	791	70	2.95	84.5	37.3	1.37 ± 0.35	116 ± 29	
GMSS-23	Ganga	Nanamau	26.8802	80.0992	8.2	131	726	50	2.92	81.7				
GMSS-25	Ganga	Haridwar	29.9416	78.1561	8.7	279	244	82	1.85	23.0	21.4			
GMSS-26	Ganga	Rishikesh	30.1032	78.2981	8.5	337	221	160	1.82	21.7	21.7	1.30 ± 0.37	73 ± 21	12
Tributaries of the Ganga														
GMSS-4	Kosi	Kursela	25.4234	87.2334	8.1	26	707	44	2.21	91.7	62.0	0.72 ± 0.15	105 ± 22	120
GMSS-5	Son	Pareo	25.5633	84.8053	8.2	62	707	12	42.4	71.3	31.8			
GMSS-7	Gandak	Sonpur	25.6915	85.1899	8.3	52	640	34	2.36	46.3	52.2	1.44 ± 0.59	129 ± 53	100
GMSS-10	Ghagra	Durgapur	25.8206	84.5905	8.1	54	1005	24	3.11	128	94.4	0.81 ± 0.26	151 ± 48	110
GMSS-19	Yamuna	Allahabad	25.4267	81.8487	8.1	93	1404	11	22.9	366	93.0			
GMSS-27	Yamuna	Ponta Sahib	30.4339	77.6257	8.8	389	100	110	2.49	7.6		0.59 ± 0.25	11.80 ± 5.00	18

Samples were obtained during a period of two weeks in Aug. 2013 (31/07/2013 to 11/08/2013).

[a]Derived from grain size data obtained from laser diffraction particle grain sizer and evaluated using GRADISTAT software (Blott and Pye, 2001).

[b]Water discharge data is taken from Rai et al. (2010) and Singh et al. (2007).

[c]"FC" are floodplain-corrected denudation rates from Lupker et al. (2012a) sampled at approximately the same location. For GMSS-1,2,3, we used the average rates from "Harding Bridge" (Fig. 1) in Lupker et al. (2012a) and for the Ganga at Rishikesh, the value given denotes the average from Lupker et al. (2012a) and Vance et al. (2003).

[d]Floodplain-corrected sediment fluxes converted from FC-*in situ* denudation rates using the source area for each basin given in Lupker et al. (2012a).

[e]From Lupker et al. (2012a) and Wittmann and von Blanckenburg (2016).

3.2 Analysis of stable ^{9}Be and meteoric ^{10}Be

Extraction of meteoric ^{10}Be and stable ^{9}Be was performed following the methods adopted from Wittmann et al. (2012). Briefly, dried suspended sediment was treated with reagents for the am-ox (0.5 M HCl), x-ox (1M hydroxylamine-hydrochloride) and residual "min" fraction (concentrated HF) sequential extraction steps. Most $[^{10}Be]_{reac}$ is hosted in the first two phases (Wittmann et al., 2012; Wittmann et al., 2015) whereas the majority of ^{9}Be is contained in the residual silicate minerals. The extracted solutions were analyzed for ^{9}Be by *Inductively Coupled Plasma-Optical Emission Spectroscopy* (ICP-OES, Varian 720-ES, Varian) on a first sample aliquot. A second aliquot was spiked with a ^{9}Be carrier. After chromatographic separation of pure Be, ^{10}Be measurements were carried out using *accelerator mass spectrometry* (AMS) at the University of Cologne, Germany (Dewald et al., 2013).

3.3 $^{9}Be_{parent}$ concentrations

We have calculated a mean $[Be]_{parent}$ value for the Ganga basin of 2.2 µg g_{rock}^{-1} by area-weighing a ^{9}Be concentration of 2.6 µg g_{rock}^{-1} for silicate rocks (Rudnick and Gao, 2004) with their Ganga basin surface area coverage (79%). The remaining 21% of the Ganga basin comprises carbonate/basaltic rocks with ^{9}Be concentrations of 0.57 µg g_{rock}^{-1}, according to Rudnick and Gao (2004). Note that the areal distributions of lithologies for the subbasins used were taken from Tripathy and Singh (2010).

Table 2: Distribution between am-ox and x-ox phases

Sample ID (GMSS-)	River	Location	Amorphous oxide-bound (am-ox)			Crystalline oxide-bound (x-ox)		
			[^{10}Be] ($\times 10^7$ at g_{solid}^{-1})	[^{9}Be] ($\mu g\ g_{solid}^{-1}$)	(^{10}Be/^{9}Be) ($\times 10^{-9}$)	[^{10}Be] ($\times 10^7$ at g_{solid}^{-1})	[^{9}Be] ($\mu g\ g_{solid}^{-1}$)	(^{10}Be/^{9}Be) ($\times 10^{-9}$)
1	Ganga	Berhampur	3.50 ± 0.12	0.505 ± 0.025	1.038 ± 0.063	0.857 ± 0.033	0.1384 ± 0.0069	0.927 ± 0.058
2	Ganga	Manikchak	3.83 ± 0.13	0.680 ± 0.034	0.842 ± 0.051	1.016 ± 0.038	0.1825 ± 0.0091	0.834 ± 0.052
3	Ganga	Bhagalpur	4.68 ± 0.16	0.500 ± 0.025	1.400 ± 0.084	0.352 ± 0.014	0.0468 ± 0.0023	1.124 ± 0.072
4	Kosi	Kursela	1.784 ± 0.061	0.506 ± 0.025	0.528 ± 0.032	0.1351 ± 0.0069	0.0402 ± 0.0020	0.502 ± 0.036
5	Son	Pareo	9.36 ± 0.31	0.599 ± 0.030	2.34 ± 0.14	1.805 ± 0.062	0.1702 ± 0.0085	1.587 ± 0.096
6	Ganga	Patna	5.69 ± 0.19	0.535 ± 0.027	1.590 ± 0.096	1.681 ± 0.060	0.1511 ± 0.0076	1.66 ± 0.10
7	Gandak	Sonpur	0.915 ± 0.033	0.258 ± 0.013	0.531 ± 0.033	0.0754 ± 0.0043	0.0226 ± 0.0011	0.499 ± 0.038
9	Ganga	Doriganj	1.507 ± 0.052	0.374 ± 0.019	0.602 ± 0.037	0.1111 ± 0.0060	0.0406 ± 0.0020	0.410 ± 0.030
10	Ghagra	Durgapur	1.611 ± 0.058	0.425 ± 0.021	0.567 ± 0.035	0.345 ± 0.016	0.1094 ± 0.0055	0.471 ± 0.032
13	Ganga	Varoli	7.31 ± 0.24	0.1523 ± 0.0076	7.18 ± 0.43	0.453 ± 0.018	0.0422 ± 0.0021	1.61 ± 0.10
14	Ganga	Gazipur	5.35 ± 0.18	0.438 ± 0.022	1.83 ± 0.11	1.524 ± 0.056	0.1307 ± 0.0065	1.74 ± 0.11
16	Ganga	Varanasi	6.41 ± 0.22	0.489 ± 0.024	1.96 ± 0.12	1.895 ± 0.068	0.1453 ± 0.0073	1.95 ± 0.12
17	Ganga	Jhansi	3.51 ± 0.12	0.707 ± 0.035	0.743 ± 0.046	0.172 ± 0.015	0.0422 ± 0.0021	0.611 ± 0.060
18	Ganga	Allhabad	9.09 ± 0.30	0.585 ± 0.029	2.33 ± 0.14	0.940 ± 0.034	0.0662 ± 0.0033	2.13 ± 0.13
19	Yamuna	Allahabad	9.45 ± 0.31	0.860 ± 0.043	1.644 ± 0.099	0.866 ± 0.031	0.0626 ± 0.0031	2.07 ± 0.13
21	Ganga	Kanpur	1.484 ± 0.054	0.377 ± 0.019	0.590 ± 0.036	0.362 ± 0.016	0.1067 ± 0.0053	0.508 ± 0.034
23	Ganga	Nanamau	1.893 ± 0.066	0.386 ± 0.019	0.734 ± 0.045	0.435 ± 0.019	0.1055 ± 0.0053	0.617 ± 0.041
25	Ganga	Haridwar	1.142 ± 0.042	0.235 ± 0.012	0.727 ± 0.045	0.175 ± 0.010	0.0506 ± 0.0025	0.517 ± 0.040
26	Ganga	Rishikesh	0.527 ± 0.020	0.1496 ± 0.0075	0.527 ± 0.033	0.0241 ± 0.0030	0.01655 ± 0.00083	0.218 ± 0.029
27	Yamuna	Ponta Sahib	3.23 ± 0.11	0.275 ± 0.014	1.75 ± 0.11	0.535 ± 0.022	0.0560 ± 0.0028	1.429 ± 0.093

All concentrations and ratios presented here are only corrected for blank, but are not corrected for sorting effects.

3.4 Sorting correction

A prerequisite for the conversion of $[^{10}Be]_{reac}$ and $[^{10}Be/^{9}Be]_{reac}$ into E and D, respectively, is that sediment samples are representative for the bulk material eroded in its source areas. However, riverine sorting likely modifies the size distribution in river sediment from that of the bulk sediment. Four effects potentially result in $[^{9}Be]_{reac}$, $[^{10}Be]_{reac}$ and $[^{9}Be]_{min}$ to differ with grain size: 1) Smaller grains offer more surface area for adsorption of dissolved ^{10}Be and ^{9}Be (Maher and von Blanckenburg, 2016; Shen et al., 2004; Willenbring and von Blanckenburg, 2010); 2) a larger grain size fraction contains more quartz that dilutes reactive Be (Wittmann et al., 2012; Wittmann et al., 2015); 3) the chemical and mineralogical composition of the reactive surfaces differs with grain size (Singleton et al., 2017; Wittmann et al., 2012), leading to co-precipitation and adsorption of variable amounts of reactive Be; 4) different grain size fractions are sourced in different depths of the weathering zone, have experienced a range of weathering intensities and erosion rates, or have

been subject to different periods of floodplain storage that lead to a change in $[^{9}Be]_{reac}$, $[^{10}Be]_{reac}$ and $[^{9}Be]_{min}$.

Only effects 1) and 2) truly introduce a grain-size dependence and will affect $^{10}Be_{reac}$ and $^{9}Be_{reac}$ alike. This grain size dependence cancels out for the $(^{10}Be/^{9}Be)_{reac}$ ratio. The grain size dependence does affect the calculation of erosion rates from $[^{10}Be]_{reac}$ (equation 1), the calculation of ^{10}Be sedimentary ^{10}Be fluxes (equation 5) from reactive ^{10}Be concentrations, and the ^{9}Be distribution between the residual phase and the reactive phase and can thus potentially bias the mobilized ^{9}Be fraction $f_{reac}^{9Be} + f_{diss}^{9Be}$ (equation 3), which in turn may affect denudation rates calculated from equation 2.

Effects 3) and 4), that we call here “geological effects”, can introduce non-systematic scatter into the grain size dependence, and can shift all isotope concentrations independently from each other, and do not cancel out for the $(^{10}Be/^{9}Be)_{reac}$ ratio. An approach to correct for these effects is by defining “representative” depth-integrated suspended sediment properties from multiple samples over a river depth profile for which a characteristic Al/Si ratio can be identified (Bouchez et al., 2011). This “representative” depth-integrated Al/Si can then be used to assign representative reactive $[^{9}Be]_{reac}$ and $[^{10}Be]_{reac}$ values (Wittmann et al., 2015). However, in the present study neither depth-profile sampling nor measurements of Al/Si were performed. We thus employed a correction procedure for the grain size effects 1) and 2) on $[Be]_{reac}$ that is based on the entire data set and comprises the following steps. First, we consider a sample to be “representative” if the depth-integrated D_{84} is 123 µm (Lupker et al., 2011) (termed “$D_{84\text{-}depth}$” in eq. 6). Lupker et al. (2011) obtained this depth-integrated D_{84} for the Ganga at Harding Bridge (Fig. 1), which corresponds to a grain size-integrated Al/Si value of 0.23 for the Ganga at Harding

Bridge. Since a very similar grain size-integrated Al/Si value of 0.22 was obtained for Himalayan Rivers (Lupker et al., 2011), our approach should be valid for these rivers, too. Second, we used the empirical slope m between D_{84} and $[^{9}Be]_{reac}$ measured for all samples (see Table 1 for D_{84}, Table 3 for $[^{9}Be]_{reac}$) to calculate a sorting-corrected $[^{9}Be]_{reac}$* from the following relationship:

$$[\,^{9}Be]_{reac} * = m \times (D_{84-depth} - D_{84-measured}) + \,^{9}Be_{reac-measured} \quad (6)$$

In theory, a sorting-correction factor can be derived for $[^{10}Be]_{reac}$ in the same way. However, we show in section 4.2 that variations in $[^{10}Be]_{reac}$ are dominated by the "geological" effects 3) and 4). Hence a dependence of $[^{10}Be]_{reac}$ on grain size is not discernible from trends against D_{84}. Thus we calculate a sorting-corrected $[^{10}Be]_{reac}$* from sorting-corrected $[^{9}Be]_{reac}$* and the $(^{10}Be/^{9}Be)_{reac}$ ratio that is unaffected by sorting:

$$[^{10}Be]_{reac} * = \,^{9}Be_{reac} * \times \left(\frac{^{10}Be}{^{9}Be}\right)_{reac} \quad (7)$$

4 Results

4.1 Changes in sampled grain size across the basin

The trend reflected in the D_{84} is consistent with the calculated clay-sized fraction abundance. D_{84} decreases from the Ganga headwaters at Rishikesh (GMSS-26) to the lowlands in Allahabad (18) and Manikchak (2). The Yamuna at Allahabad (19) and the Son at Pareo (5) draining southern Peninsular India show the lowest D_{84} (Table 1, Fig. 2a). Below the confluences with these southern rivers, a sharp

increase of up to ~20% is recorded in the clay-sized fraction abundance, whereas the northern tributaries, i.e. Ghagra (10), Gandak (7), Kosi (4) and Yamuna (27) (in its upper reaches) show lower abundance of around 5% (Fig. 2a).

4.2 Grain size dependence and results of sorting correction

As suggested in section 3.4, a dependence of $[^{9}Be]_{reac}$ on grain size is indeed indicated from the correlation with D_{84} (Fig. 3). The slope *m* of the relationship between $[^{9}Be]_{reac}$ and D_{84} (Fig. 3a) is 0.0044 µg g^{-1}/µm. In contrast, $[^{9}Be]_{min}$ is not systematically affected by sorting (Fig. 3b). The correlation between $[^{10}Be]_{reac}$ and D_{84} (Fig. 3c) is weak, confirming that variations in $[^{10}Be]_{reac}$ are mainly governed by "geological" effects. Hence, a grain size control is not discernible from the ^{10}Be trend. We thus used equation 6 and *m* to calculate sorting-corrected $[^{9}Be]_{reac}$*. In the absence of grain size data for the sample GMSS-17 no sorting correction was carried out. Resulting sorting-correction for samples GMSS-7 and 13 yields negative $[^{9}Be]_{reac}$* values. Hence, for these three samples, we used sorting-uncorrected data for further calculations. For all other samples, we used the derived $[^{9}Be]_{reac}$* and the $(^{10}Be/^{9}Be)_{reac}$ ratio to calculate a sorting-corrected $[^{10}Be]_{reac}$* (eq. 7). These corrections remove to a first order the bias introduced by grain size effects 1) and 2), but not the "geological" effects 3) and 4) that introduce deviations from the calculated slope. These "geological" effects are introduced because we used the data from the entire Ganga basin to infer these correlations, rather than using correlations on grain size fractions from a single sample or a depth profile (Wittmann et al., 2015). We thus regard an error propagation from the scatter around this slope on the correction of D and E not as justified, as it would add an uncertainty into the data that does not result from grain size dependence.

Below we use sorting-corrected $[^{10}Be]_{reac}$* throughout to calculate sorting-corrected E* and delivery flux ratios $J_{riv}^{^{10}Be*}$. We used sorting-corrected $[^{9}Be]_{reac}$* to calculate sorting-corrected $f_{reac}^{9Be} + f_{diss}^{9Be*}$, which in turn we use to calculate sorting-corrected D_{met}*. In most samples, $[^{9}Be]_{reac}$ and $[^{10}Be]_{reac}$ decrease by a factor of 2 after applying this correction (Table 3), and correspondingly E and D increase by a factor of ca. 2.

Table 3: Results of ^{9}Be and ^{10}Be concentration measurements and ^{10}Be/^{9}Be ratios with sorting-corrections.

Sample ID (GMSS-)	River	Location	Initial sample weight (g)	$[^{9}Be]_{reac}$			$[^{9}Be]_{min}$	$[^{10}Be]_{reac}$		$(^{10}Be/^{9}Be)_{reac}$
				$[^{9}Be]$ (µg g_{solid}^{-1})	Sorting-corr. $[^{9}Be]_{reac}$* (µg g_{solid}^{-1}) [a]		$[^{9}Be]_{min}$ (µg g_{solid}^{-1})	$[^{10}Be]_{reac}$ (×10^{7} at g_{solid}^{-1}) [b]	Sorting-corr. $[^{10}Be]_{reac}$* (×10^{7} at g_{solid}^{-1}) [c]	($^{10}Be/^{9}Be)_{reac}$ (×10^{-8})
1	Ganga	Berhampur	0.6137	0.644 ± 0.026	0.374 ± 0.015		1.411 ± 0.071	4.36 ± 0.13	2.533 ± 0.073	1.014 ± 0.051
2	Ganga	Manikchak	0.5912	0.863 ± 0.035	0.440 ± 0.017		1.405 ± 0.070	4.85 ± 0.14	2.471 ± 0.070	0.841 ± 0.042
3	Ganga	Bhagalpur	1.0671	0.547 ± 0.025	0.262 ± 0.017		1.160 ± 0.058	5.03 ± 0.16	2.406 ± 0.075	1.376 ± 0.076
4	Kosi	Kursela	0.9812	0.546 ± 0.025	0.246 ± 0.016		1.540 ± 0.077	1.919 ± 0.062	0.864 ± 0.028	0.526 ± 0.030
5	Son	Pareo	0.9437	0.769 ± 0.031	0.346 ± 0.031		0.939 ± 0.047	11.16 ± 0.32	5.02 ± 0.14	2.17 ± 0.11
6	Ganga	Patna	0.6472	0.687 ± 0.028	0.364 ± 0.018		1.107 ± 0.055	7.37 ± 0.20	3.90 ± 0.11	1.607 ± 0.079
7	Gandak	Sonpur	1.0238	0.280 ± 0.013	-		1.682 ± 0.084	0.990 ± 0.033	-	0.529 ± 0.030
9	Ganga	Doriganj	0.9736	0.415 ± 0.019	0.107 ± 0.013		1.411 ± 0.071	1.618 ± 0.052	0.418 ± 0.013	0.584 ± 0.032
10	Ghagra	Durgapur	0.6282	0.534 ± 0.022	0.158 ± 0.012		1.715 ± 0.086	1.956 ± 0.060	0.579 ± 0.018	0.548 ± 0.028
13	Ganga	Varoli	1.0521	0.1944 ± 0.0079	-		0.910 ± 0.046	7.76 ± 0.24	-	5.97 ± 0.31
14	Ganga	Gazipur	0.5839	0.568 ± 0.023	0.466 ± 0.020		1.076 ± 0.054	6.88 ± 0.19	5.63 ± 0.16	1.810 ± 0.088
16	Ganga	Varanasi	0.6104	0.634 ± 0.026	0.342 ± 0.017		1.056 ± 0.053	8.30 ± 0.23	4.47 ± 0.12	1.958 ± 0.095
17	Ganga	Jhansi	0.2343	0.750 ± 0.035	-		1.562 ± 0.078	3.68 ± 0.13	-	0.735 ± 0.043
18	Ganga	Allhabad	1.0040	0.651 ± 0.029	0.225 ± 0.014		0.758 ± 0.038	10.03 ± 0.30	3.47 ± 0.11	2.31 ± 0.13
19	Yamuna	Allahabad	1.0580	0.923 ± 0.043	0.495 ± 0.020		0.701 ± 0.035	10.32 ± 0.32	5.54 ± 0.17	1.673 ± 0.093
21	Ganga	Kanpur	0.6545	0.483 ± 0.020	0.282 ± 0.015		1.455 ± 0.073	1.846 ± 0.056	1.077 ± 0.033	0.571 ± 0.029
23	Ganga	Nanamau	0.6320	0.491 ± 0.020	0.214 ± 0.014		1.555 ± 0.078	2.328 ± 0.069	1.014 ± 0.030	0.709 ± 0.036
25	Ganga	Haridwar	0.6096	0.286 ± 0.012	0.1300 ± 0.0095		1.628 ± 0.081	1.317 ± 0.043	0.599 ± 0.020	0.690 ± 0.037
26	Ganga	Rishikesh	1.0112	0.1661 ± 0.0075	0.3067 ± 0.0078		1.575 ± 0.079	0.551 ± 0.020	1.017 ± 0.037	0.496 ± 0.029
27	Yamuna	Ponta Sahib	0.6321	0.331 ± 0.014	0.282 ± 0.012		1.623 ± 0.081	3.76 ± 0.11	3.20 ± 0.10	1.700 ± 0.088

For all ^{9}Be concentrations, a 5% uncertainty from the ICP-OES repeatability was propagated through all further calculations. All uncertainties are 1σ uncertainties. For sorting-corrected $[^{9}Be]_{reac}$, no additional uncertainty was propagated, but the relative analytical uncertainty of uncorrected $[^{9}Be]_{reac}$ was used.

[a] Sorting correction was done by using the empirical slope between D_{84} and $[^{9}Be]_{reac}$ (derived from all samples; equation 6) relative to a grain size-integrated Al/Si ratio of 0.23 that corresponds to a representative D_{84} of 123 µm (Lupker et al., 2011). Note that no grain size data is available for samples GMSS-17 and that the sorting correction would result in negative values for GMSS-7 and -13, such that we use uncorrected values for these three samples throughout the manuscript.

[b] A blank ratio of 7.5±4.8x10^{-16} (n=8) was subtracted from measured AMS ratios, and the error was propagated into ^{10}Be concentrations.

[c] Sorting-corrected ^{10}Be concentrations were calculated from multiplying sorting-corrected $[^{9}Be]_{reac}$ with $(^{10}Be/^{9}Be)_{reac}$.

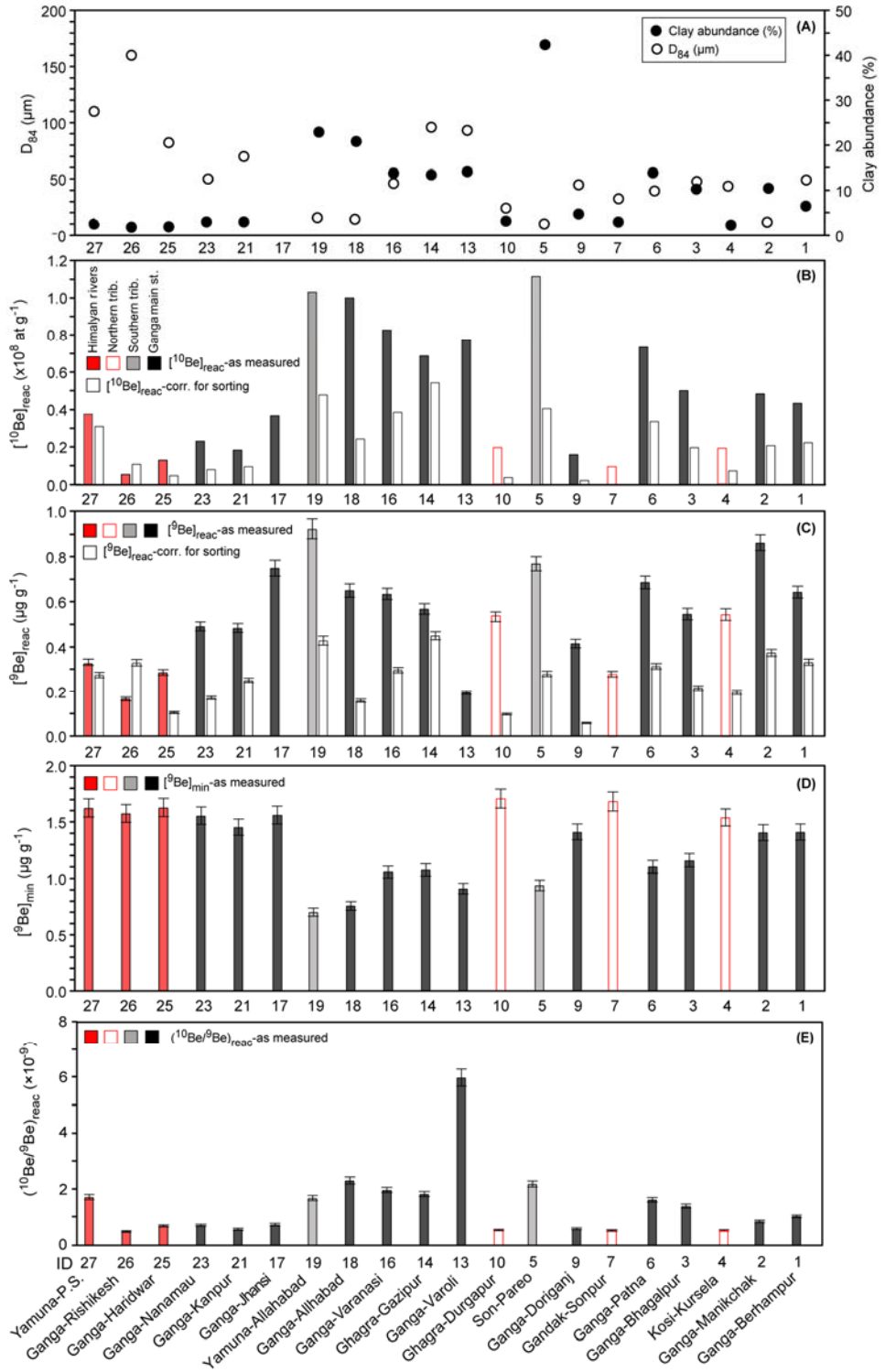

Figure 2) A) Grain size parameters D_{84} (in µm, white circles) and clay-sized abundance (in %, black circles), B) $[^{10}Be]_{reac}$ ($\times 10^8$ at g_{solid}^{-1}), C) $[^{9}Be]_{reac}$ (in µg g^{-1}), D) $[^{9}Be]_{min}$ (in µg g^{-1}), and E) $(^{10}Be/^{9}Be)_{reac}$ ($\times 10^{-9}$) for all samples aligned along main stem from source to lowlands (numbers give GMSS-ID; "Yamuna P.S." is the Yamuna at Ponta Sahib). Colored bars are data as measured; in case of $[^{10}Be]_{reac}$* and $[^{9}Be]_{reac}$* data, a sorting-correction was done (white bars in B and C; Sections 3.4 and 4.2). Shown uncertainties as given in Table 3 (if no uncertainty is shown it means that uncertainty is contained within symbol).

4.3 Trends in ^{9}Be and ^{10}Be concentrations from headwaters to lowlands

We find three-fold lower sorting-corrected $[^{10}Be]_{reac}$* in the northern and Himalaya-draining rivers (average 1.2×10^{7} at g_{solid}^{-1}, n = 6) compared to the Ganga main stem samples in the lowlands (average 3.3×10^{7} at g_{solid}^{-1}, n = 11). This $[^{10}Be]_{reac}$* of main stem Ganga samples is noticeably affected by high $[^{10}Be]_{reac}$* from the southern rivers draining cratonic Peninsular India. After the confluence with the Yamuna, the downstream Ganga main stem samples become elevated in $[^{10}Be]_{reac}$*, with a 3-fold higher $[^{10}Be]_{reac}$* at GMSS-18 compared to GMSS-26 to 21. $[^{10}Be]_{reac}$* stays elevated along the floodplain course, with only a temporal decrease in $[^{10}Be]_{reac}$* at GMSS-9 after the Ghagra inflow, a northern (Himalaya-draining) tributary. This sample, and to some extent the GMSS-6 at Patna, yield anomalous $[^{10}Be]_{reac}$* compared to their neighbouring main stem samples. This effect may be caused by their proximity to confluences (5-10 km) where poorly mixed sediment locally dominates. Sorting-corrected $[^{9}Be]_{reac}$* shows less variability, and is ca. 30% to 50% higher in the lowland Ganga main stem samples (mean of 0.33 µg g^{-1}) and in the southern rivers draining cratonic Peninsular India (mean of 0.42 µg g^{-1}, n = 2), respectively, than in northern and Himalaya-draining rivers (mean of 0.23 µg g^{-1}). Resulting $(^{10}Be/^{9}Be)_{reac}$ ratios are low (ca. 0.75×10^{-9}) in northern/Himalayan-draining tributaries, increase across the floodplain (ca. 1.7×10^{-9} for Ganga main stem samples) and are the highest in the southern rivers draining the cratonic Peninsular India (1.9×10^{-9}, average of samples GMSS-5 and 19). $(^{10}Be/^{9}Be)_{reac}$ is ca. 0.8×10^{-9} at the furthest downstream Ganga at Manikchak (GMSS-2).

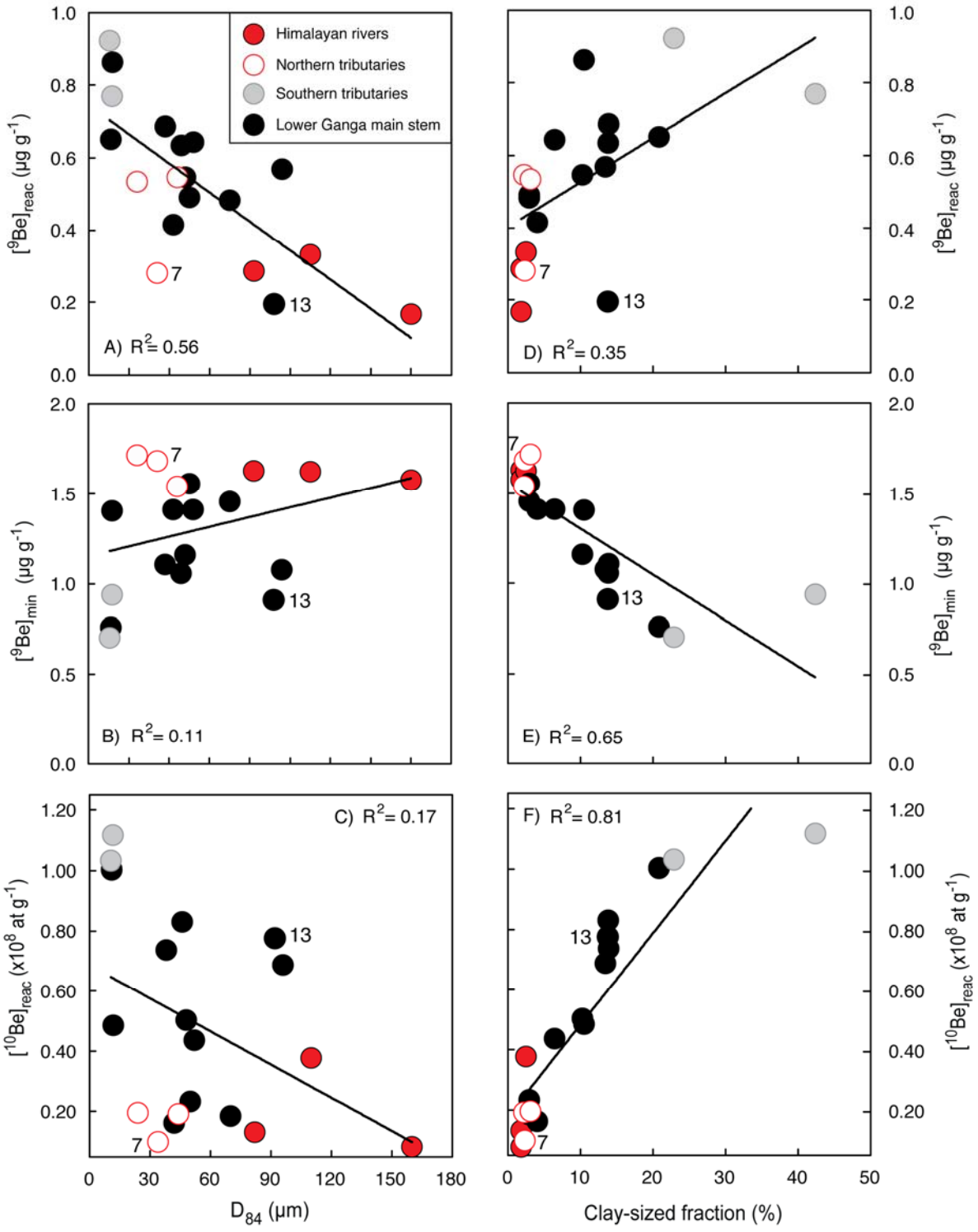

Figure 3) A) $[^{9}Be]_{reac}$(in µg g^{-1}), B) $[^{9}Be]_{min}$ (in µg g^{-1}), and C) $[^{10}Be]_{reac}$ (×10^{8} at g_{solid}^{-1}) versus grain size parameter D_{84} (in µm) and D) $[^{9}Be]_{reac}$ (in µg g^{-1}) , E) $[^{9}Be]_{min}$ (in µg g^{-1}), and F) $[^{10}Be]_{reac}$ (×10^{8} at g_{solid}^{-1}) versus clay abundance (in %). Note that GMSS-17 is not plotted due to absence in grain size data, and GMSS-7 and -13 are indicated by ID, as a sorting-correction for these samples would result in negative values. Hence for these samples, sorting-uncorrected ^{9}Be and ^{10}Be data were used throughout.

5 Discussion of ^{9}Be and ^{10}Be concentrations and ^{10}Be fluxes

5.1 Balance of ^{10}Be depositional and export fluxes

To test whether the ^{10}Be exported from the sedimentary flux $J_{riv}^{^{10}Be*}$ is at steady state with respect to the atmospheric ^{10}Be flux, $J_{atm}^{^{10}Be}$ (both in at yr^{-1}), we have calculated a flux balance using $[^{10}Be]_{reac}$* (Table 4) based on equations 4 and 5, following the approach of Wittmann et al. (2015).

For six Ganga main stem locations and four tributaries (Table 4), the erosion rate E in equation 5 can be independently estimated from river load gauging (Lupker et al., 2012a; Wittmann and von Blanckenburg, 2016) (yielding $J_{riv}^{^{10}Be*}$, in at yr^{-1}) or from floodplain-corrected *in situ*-derived denudation rates (Lupker et al., 2012a) ($J_{riv-insitu}^{^{10}Be*}$, in at yr^{-1}). The exported sedimentary to depositional flux ratio $J_{riv}^{^{10}Be*}/J_{atm}^{^{10}Be}$, scatters between 0.4 and 4 for the upstream samples and converges to ca. 1 for samples downstream of Patna (GMSS-6) (Fig. 4). Using *in situ* ^{10}Be-derived export fluxes for $J_{riv}^{^{10}Be*}$, $J_{riv-insitu}^{^{10}Be*}/J_{atm}^{^{10}Be}$ ratios are closer to 1 than those derived from gauging. Sediment fluxes from gauging are generally lower than those by *in situ* ^{10}Be, a finding supported by Lupker et al. (2012a), thus yielding lower $J_{riv-gaug}^{^{10}Be*}/J_{atm}^{^{10}Be}$ (Fig. 4). One exception is the upper Yamuna (GMSS-27), where a relatively high gauging-derived sediment flux (that is similar to in the *in situ*-derived sediment flux, Table 1) results in a high $J_{riv-gaug}^{^{10}Be*}/J_{atm}^{^{10}Be}$. We regard sediment fluxes from *in situ* ^{10}Be and therefore also $J_{riv-insitu}^{^{10}Be*}/J_{atm}^{^{10}Be}$ to be more reliable than those from gauging because a) gauging-derived fluxes from surface sediment sampling are frequently biased towards both higher or lower values by events of short integration period such as flash floods or land use change, or by sediment trapping behind dams, respectively,

and b) *in situ* ^{10}Be accumulates over similar time scales as sediment-bound meteoric ^{10}Be. Although the integration time scale of meteoric ^{10}Be cannot be calculated assuming a fixed attenuation depth as it is the case for *in situ* ^{10}Be-derived denudation rates, Willenbring and von Blanckenburg (2010) proposed that the meteoric adsorption coefficient *k*, 1/cm, is a function of soil depth. Assuming thin soils and rapid erosion rates in the Himalayas, i.e. for an *in situ* ^{10}Be-derived denudation rate range of 0.7 to 1.2 mm yr^{-1} characteristic for the upper Yamuna and Ganga river basins, respectively (values from Wittmann & von Blanckenburg, 2016) and an assumed mean Himalayan soil depth of <50 cm (Sarkar et al., 2013), we estimate an integration time scale range of 0.4 to 0.7 kyr for these Himalayan catchments. Given that the attenuation depth for *in situ* ^{10}Be is fixed to 60 cm, the integration time scales for both methods should be similar. Given this, short-term transient perturbation such as land use changes in the recent past are most likely not resolvable by both cosmogenic methods, but such perturbations most likely affect gauging-based methods.

An underestimation of $F_{met}^{^{10}Be}$ may explain excessive $J_{riv}^{^{10}Be*}/J_{atm}^{^{10}Be}$ (>1, Fig. 4). Orographic effects might cause the ^{10}Be flux to be a function of the precipitation rate (Willenbring and von Blanckenburg, 2010), thereby affecting estimates of $F_{met}^{^{10}Be}$ in the Himalayas which may thus be inaccurately represented in the flux model used. Such an “additive” effect is expected to be averaged-out on large spatial scales of the Ganga lowlands (Wittmann et al., 2015). Indeed, uncertainties in the atmospheric flux models are the largest in the higher Himalayas (Fig. 4, grey shaded area), where the distribution maps (Heikkilä and von Blanckenburg, 2015) show the largest differences up to a factor of 2 between the modern and the early Holocene GCM model runs (see Supplement S1).

The exported sedimentary to depositional ^{10}Be flux ratio being close to or slightly exceeding unity contrasts with the Amazon basin, where this ratio is mostly between 0.3 and 0.8 (Wittmann et al., 2015). In the Amazon basin radioactive decay of ^{10}Be during extended (Myr-time scale) sediment storage was identified as cause for this mismatch (Wittmann et al., 2015). Hence in the Ganga, time scales of sediment storage are predicted to be much shorter than the half-life of ^{10}Be. A maximum sediment turnover time of 470 kyr was suggested by Métivier and Gaudemer (1999) for the Ganga basin by assessing the dimensions of the total floodplain reservoir (sediment volume = 9×10^4 km^3) divided by the annual sediment flux (0.19 km^3 yr^{-1}). According to Lupker et al. (2012a) who used the dimensions of the active floodplain for a similar calculation, the transfer time of sediment from the Himalayas to the outlet is 1.4 kyr.

Table 4: Depositional fluxes, ^{10}Be mass balance, weathering intensities, erosion and denudation rates

ID	Depositional meteoric flux $F^{10}Be_{met}$ [a]	*^{10}Be mass balance*					*Weathering proxy from ^{9}Be*		Erosion rate E_{met}*			Denudation rate D_{met} and D_{met}*					
		$J^{10}Be_{atm}$ [b]	Int.1σ	Ext.1σ	$J^{10}Be_{riv\text{-}insitu}$* [c]	$J^{10}Be_{riv\text{-}gaug}$* [c]	$(f_{reac}+f_{diss})$	$(f_{reac}+f_{diss})$* [d]	(sorting-corr.)[e]	Int.1σ	Ext.1 σ	(uncorr.)[f]	Int.1σ	Ext.1σ	(sorting-corr.)[g]	Int.1σ	Ext.1σ
	(×10^{6} at cm^{-2} yr^{-1})	(×10^{22} at yr^{-1})					(measured)	(sorting-corr.)	(mm yr^{-1})			(mm yr^{-1})			(mm yr^{-1})		
1	1.09 ± 0.75				-	-	0.31 ± 0.12	0.209 ± 0.080	0.1653	0.0048	0.1141	0.0896	0.0048	0.0521	0.1341	0.0072	0.0780
2	1.09 ± 0.76	1.020	0.102	0.708	0.9635 ± 0.0055	1.2948 ± 0.0070	0.38 ± 0.14	0.238 ± 0.085	0.1698	0.0048	0.1179	0.0893	0.0048	0.0524	0.1425	0.0077	0.0836
3	1.05 ± 0.70	0.869	0.087	0.585	1.45 ± 0.15	1.2609 ± 0.0075	0.32 ± 0.15	0.184 ± 0.086	0.1674	0.0052	0.1128	0.0622	0.0037	0.0351	0.1082	0.0065	0.0611
4	1.37 ± 1.02	0.126	0.013	0.094	0.724 ± 0.073	0.09100 ± 0.00062	0.26 ± 0.12	0.138 ± 0.065	0.610	0.020	0.4555	0.261	0.016	0.174	0.496	0.030	0.331
5	0.85 ± 0.17				-	-	0.45 ± 0.19	0.27 ± 0.11	0.0649	0.0019	0.0132	0.0227	0.0012	0.0033	0.0379	0.0020	0.0055
6	1.05 ± 0.72	0.814	0.081	0.562	1.21 ± 0.12	0.9861 ± 0.0063	0.38 ± 0.15	0.247 ± 0.098	0.1034	0.0028	0.0714	0.0446	0.0024	0.0259	0.0691	0.0037	0.0401
7	2.00 ± 2.09	0.0927	0.0093	0.0969	1.38 ± 0.14	0.1278 ± 0.0018	0.143 ± 0.063	-	*0.777*	*0.026*	*0.813*	0.694	0.043	0.837	-	-	-
9	1.04 ± 0.75				-	-	0.23 ± 0.15	0.071 ± 0.048	0.961	0.031	0.691	0.206	0.012	0.129	0.663	0.040	0.416
10	1.11 ± 0.74	0.142	0.014	0.094	0.612 ± 0.062	0.08725 ± 0.00085	0.24 ± 0.13	0.084 ± 0.045	0.740	0.023	0.490	0.224	0.012	0.122	0.630	0.035	0.343
13	1.04 ± 0.76				-	-	0.176 ± 0.090	-	*0.0518*	*0.0016*	*0.0377*	0.0260	0.0014	0.0166	-	-	-
14	1.04 ± 0.76				-	-	0.35 ± 0.13	0.30 ± 0.11	0.0713	0.0020	0.0519	0.0437	0.0023	0.0277	0.0500	0.0026	0.0317
16	1.04 ± 0.76	0.489	0.049	0.356	0.431 ± 0.043	0.2108 ± 0.0012	0.38 ± 0.15	0.245 ± 0.099	0.0898	0.0025	0.0654	0.0372	0.0020	0.0236	0.0571	0.0030	0.0362
17	1.04 ± 0.76				-	-	0.32 ± 0.10	-	*0.1091*	*0.0037*	*0.0795*	0.1146	0.0072	0.0738	-	-	-
18	1.04 ± 0.76				-	-	0.46 ± 0.24	0.23 ± 0.12	0.1158	0.0035	0.0843	0.0257	0.0015	0.0164	0.0518	0.0031	0.0331
19	0.73 ± 0.34				-	-	0.57 ± 0.23	0.41 ± 0.17	0.0505	0.0015	0.0234	0.0200	0.0012	0.0065	0.0275	0.0017	0.0089
21	1.04 ± 0.80	0.0878	0.0088	0.0678	1.43 ± 0.14	0.1254 ± 0.0010	0.25 ± 0.11	0.162 ± 0.068	0.371	0.011	0.287	0.1908	0.0104	0.1340	0.293	0.016	0.206
23	1.08 ± 0.80				-	-	0.24 ± 0.11	0.121 ± 0.057	0.410	0.012	0.305	0.1662	0.0091	0.1093	0.330	0.018	0.217
25	1.29 ± 1.40				-	-	0.149 ± 0.089	0.074 ± 0.044	0.829	0.027	0.901	0.328	0.019	0.423	0.662	0.038	0.854
26	1.50 ± 1.40	0.0330	0.0033	0.0309	2.26 ± 0.23	0.07457 ± 0.00078	0.095 ± 0.040	0.163 ± 0.069	0.568	0.021	0.531	0.830	0.052	0.819	0.486	0.030	0.480
27	1.46 ± 1.33	0.0140	0.0014	0.0128	2.69 ± 0.27	0.03766 ± 0.00049	0.170 ± 0.072	0.148 ± 0.063	0.1754	0.0053	0.1601	0.1326	0.0075	0.1247	0.1519	0.0086	0.1428

[a] Basin-wide meteoric ^{10}Be flux calculated for each basin on SRTM-pixel basis using the average from an industrial (modern) and a pre-industrial (Holocene) model run (Heikkilä et al., 2013a,b). Dataset is available online (DOI: 10.5880/GFZ.3.4.2015.001). Uncertainty is difference between two model runs. Note that we propagated this external uncertainty only when comparing to external data.

[b] Calculated using eq. 4; given uncertainties are a 10% arbitrary internal uncertainty on $F^{10}Be_{met}$ and the external uncertainty on $F^{10}Be_{met}$ resulting from the difference in the two model runs.

[c] Calculated using eq. 5 (with *in situ*-derived or gauging-derived sediment fluxes); given uncertainties include an arbitrary uncertainty of 10% and 20% for the depositional flux and gauging data, respectively, and uncertainty for *in situ* data given in Table 1. All J_{riv}´s were calculated using grain size-corrected ^{10}Be concentrations.

[d] Calculated according to eq. 3 using sorting-corrected $[^{9}Be]_{reac}$. Uncertainties are propagated analytical uncertainties of all concentrations and those of *in situ*- derived sediment fluxes (see Table 1) where appropriate.

[e] Calculated using eq. 1 using sorting-corrected $[^{10}Be]_{reac}$; internal uncertainty is composed of 10% uncertainty on $F^{10}Be_{met}$ and analytical uncertainties; external uncertainty uses the external uncertainty on $F^{10}Be_{met}$. Italic values give E_{met} (not sorting-corrected).

[f] Calculated using eq. 2 using $(f_{reac}+f_{diss})$ not corrected for sorting (and using same uncertainty treatment as in subscript g).

[g] Calculated using eq. 2 using sorting-corrected $(f_{reac}+f_{diss})$*; internal uncertainty is composed of 10% uncertainty on $F^{10}Be_{met}$ and analytical uncertainties; external uncertainty contains the external uncertainty on $F^{10}Be_{met}$, analytical uncertainties and a 0.5 µg g_{solid}^{-1} uncertainty for $[^{10}Be]_{parent}$.

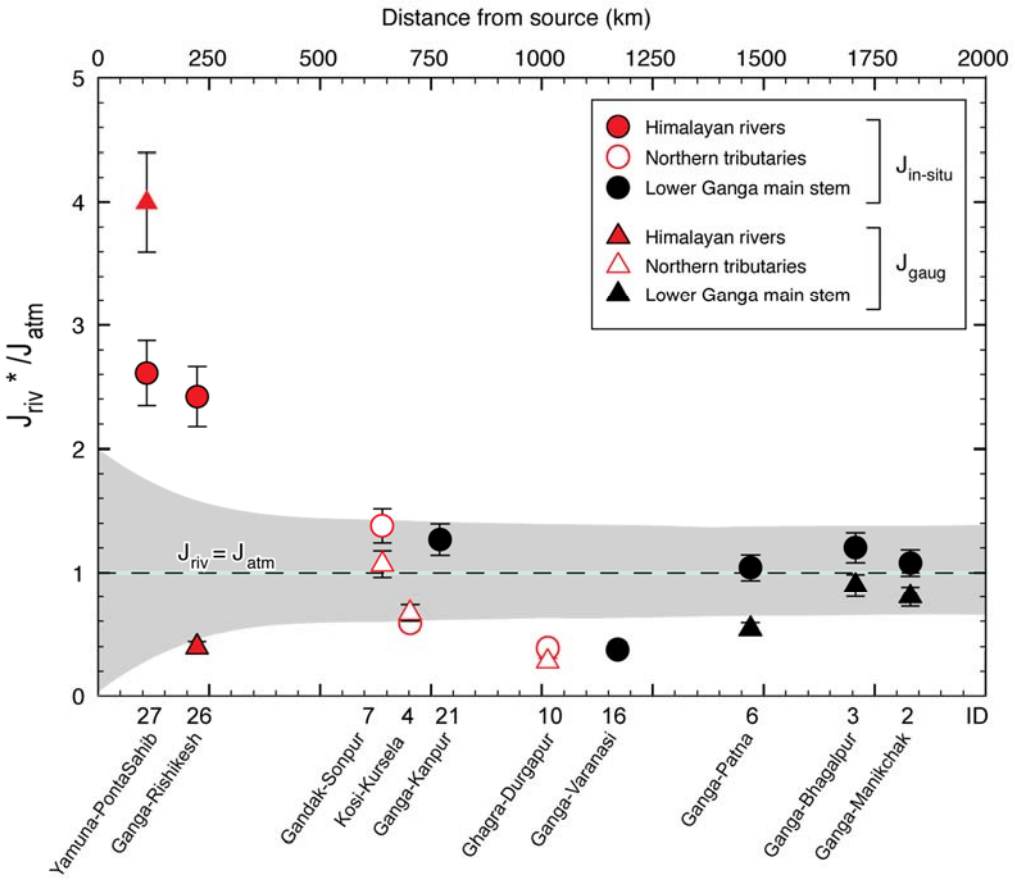

Figure 4) Ratio of sedimentary ^{10}Be export $J_{riv}^{^{10}Be*}$ versus ^{10}Be deposition $J_{atm}^{^{10}Be}$ for several Ganga main stem locations (black symbols) and for several northern and Himalayan-draining tributaries (red/open symbols). Triangles denote $J_{riv-gaug}^{^{10}Be*}$ calculated using gauging-derived E in eq. 5 and circles denote $J_{riv-insitu}^{^{10}Be*}$ calculated using floodplain-corrected *in situ* ^{10}Be-derived E in eq. 5. Balanced erosional and depositional ^{10}Be fluxes equal a ratio of $J_{riv}^{^{10}Be*}$ to $J_{atm}^{^{10}Be}$ of 1 (stippled line). We used $[^{10}Be]_{reac}$* and $F_{met}^{^{10}Be}$ from Table 4, of which the analytical uncertainties were propagated. The grey shaded area shows the uncertainty associated with J_{atm} from the comparison of an early Holocene with an industrial climate model (Heikkilä & von Blanckenburg, 2015), which denotes to ca. 100% in the Himalayas (see Supplement S1) and ca. 40-50% in the Ganga lowlands (Table 4).

5.2 Equilibration between amorphous and crystalline oxide phases

[^{9}Be] and [^{10}Be] of the am-ox phase exceed that contained in the x-ox phase by on average a factor of 10 (Table 2). Proportions of [^{9}Be] and [^{10}Be] between the two leached phases are similar, such that (^{10}Be/^{9}Be)$_{am\text{-}ox}$ and (^{10}Be/^{9}Be)$_{x\text{-}ox}$ ratios agree well (Table 2). This behavior differs strongly to that observed in the Amazon (Wittmann et al., 2015). There, amorphous-bound ^{9}Be amounts roughly equals crystalline-bound amounts. Also in the Amazon floodplain, amorphous-bound ^{10}Be increases more than ^{9}Be such that higher amorphous ^{10}Be/^{9}Be emerged. The high crystalline oxide concentration was interpreted to have formed during extended ageing in the eroding soils, whereas the increase in amorphous oxides was attributed to storage in the lowlands (Wittmann et al., 2015). In the Himalayan source areas of the Ganga, in contrast, erosion rates are higher, thus less time is available for formation of crystalline oxides, and sediment storage time in the lowland basin is much shorter, so that the accumulation of amorphous-bound ^{10}Be is not resolvable. Hence, the trends in the distribution of ^{10}Be among the different phases can be linked to actual processes in each setting.

6 Weathering intensities, erosion rates and denudation rates

6.1 The mobilized fraction $f_{reac}^{9Be} + f_{diss}^{9Be}$ as an index of weathering intensity

We use the flux fraction of ^{9}Be $f_{reac}^{9Be} + f_{diss}^{9Be}$ that is released during weathering of primary minerals and partitioned either into the reactive or into the dissolved phases as a proxy for the intensity of chemical weathering (von Blanckenburg et al., 2012).

The weathering intensity $(f_{reac}^{9Be} + f_{diss}^{9Be}) *$ (calculated using eq. 3 and corrected for sorting) encompasses a range from 0.071 to 0.41. The weathering fraction decreases with denudation rate (Fig. 5), with the lowest mobilized Be fractions of

0.13 found in the northern and Himalaya-draining rivers (average of GMSS-4,10, 25-27; n = 5; note that we do not consider non-grain size corrected samples here) relative to higher mobilized fractions of ca. 0.34 in craton-draining rivers (average of samples GMSS-5 and 19), whereas the Ganga main stem samples comprise a mix of these two "end members" with an average $(f_{reac}^{9Be} + f_{diss}^{9Be}) *$ of 0.20 (n = 9) falling between these two estimates. A possible increase in $(f_{reac}^{9Be} + f_{diss}^{9Be}) *$ across the downstream Ganga floodplain (such as the one observed across the Amazon Basin; Wittmann et al., 2015) is not discernable as it is obscured by the overall variability in $(f_{reac}^{9Be} + f_{diss}^{9Be}) *$. Some of this variability is introduced by tributary admixing with high $(f_{reac}^{9Be} + f_{diss}^{9Be}) *$ values from southern and low values from northern tributaries, respectively.

The observation that the weathering fraction decreases with denudation rate from the Himalayan headwaters into the floodplain can be explained with weathering kinetics. Higher $f_{reac}^{9Be} + f_{diss}^{9Be}$ are expected in slowly eroding terrains, whereas lower $f_{reac}^{9Be} + f_{diss}^{9Be}$ characterize rapidly eroding terrains in which erosion outpaces weathering kinetics (von Blanckenburg et al., 2012). That $f_{reac}^{9Be} + f_{diss}^{9Be}$ does not increase resolvably in the floodplain is also expected. Based on the net Si flux combined with Si stable isotopes, the estimates of Si release from weathering in the Ganga floodplain has been estimated to amount to ca. 55 Gmoles yr^{-1}, ca. 30 Gmoles yr^{-1} of which are sequestered into secondary phases (Frings et al., 2015). Similar amounts of Na, K, and Mg were reported to be released from silicate weathering in the Ganga plain (Lupker et al., 2012b). 55 Gmoles yr^{-1} Si correspond to ca. 1.4×10^6 t yr^{-1}. The total sediment flux through the Ganga plain however is ca. $600\text{-}700 \times 10^6$ t yr^{-1}. Thus, the fraction of elements released during weathering is low, and explains the absence of increase in $f_{reac}^{9Be} + f_{diss}^{9Be}$.

The range in $f_{reac}^{9Be} + f_{diss}^{9Be}$ found in the Ganga floodplain is towards the lower end of observations from global rivers that have been estimated to range between 0.2 to 0.3 (von Blanckenburg et al., 2012), and between 0.3 to 0.4 in the Amazon basin (Wittmann et al., 2015). However, the value for the Himalayas is at the low end of the global range.

6.2 Erosion rates from $[^{10}Be]_{reac}$ and denudation rates from $(^{10}Be/^{9}Be)_{reac}$ ratios

Sorting-corrected erosion rates E_{met}* (mm yr^{-1}) in the Ganga basin calculated using equation 1 are within a factor of 2 of denudation rates D_{met}* (mm yr^{-1}; calculated from sorting-corrected $(f_{reac}^{9Be} + f_{diss}^{9Be}) *$ in equation 2 where possible, Table 4, Fig. 6A). Note that we present for completeness a comparison of sorting- versus non-sorting corrected E and D in the supplement (Fig. S1).

For most samples, E exceeds D by up to a factor of 2 (Fig. 6A). This excess is not possible as D comprises the sum of E and W. We can exclude an over- or under-estimation in $F_{met}^{10_{Be}}$ which would affect E and D alike. An overestimate of $[^{9}Be]_{parent}$ is one possible explanation, given that lithologies in the Ganga source areas are heterogeneous with respect to ^{9}Be concentrations. As an example we have indicated with an arrow in Fig. 6A how D_{met}* would shift if $[^{9}Be]_{parent}$ were 1.5 µg g^{-1} instead of our lithology-weighed value of 2.2 µg g^{-1}. Another explanation is that the sorting correction does not accurately capture $[^{10}Be]_{reac}$. An underestimate of sorting-corrected $[^{10}Be]_{reac}$* by a factor of ca. 2 might explain the excess in erosion rate.

The observation of E being similar to D was made in the Amazon basin (Wittmann et al., 2015). In that study both E and D were determined from depth-integrated river profiles, thus a bias on $[^{10}Be]_{reac}$ from sorting could be excluded. The agreement between E and D in the Amazon basin was attributed to the degree of weathering of

the mostly sedimentary and hence pre-weathered lithologies of the basin. In the Ganga, in contrast, samples with similar E and D testify to the low degree of weathering that results from the rapid, kinetically limited Himalayan denudation regime and low floodplain weathering.

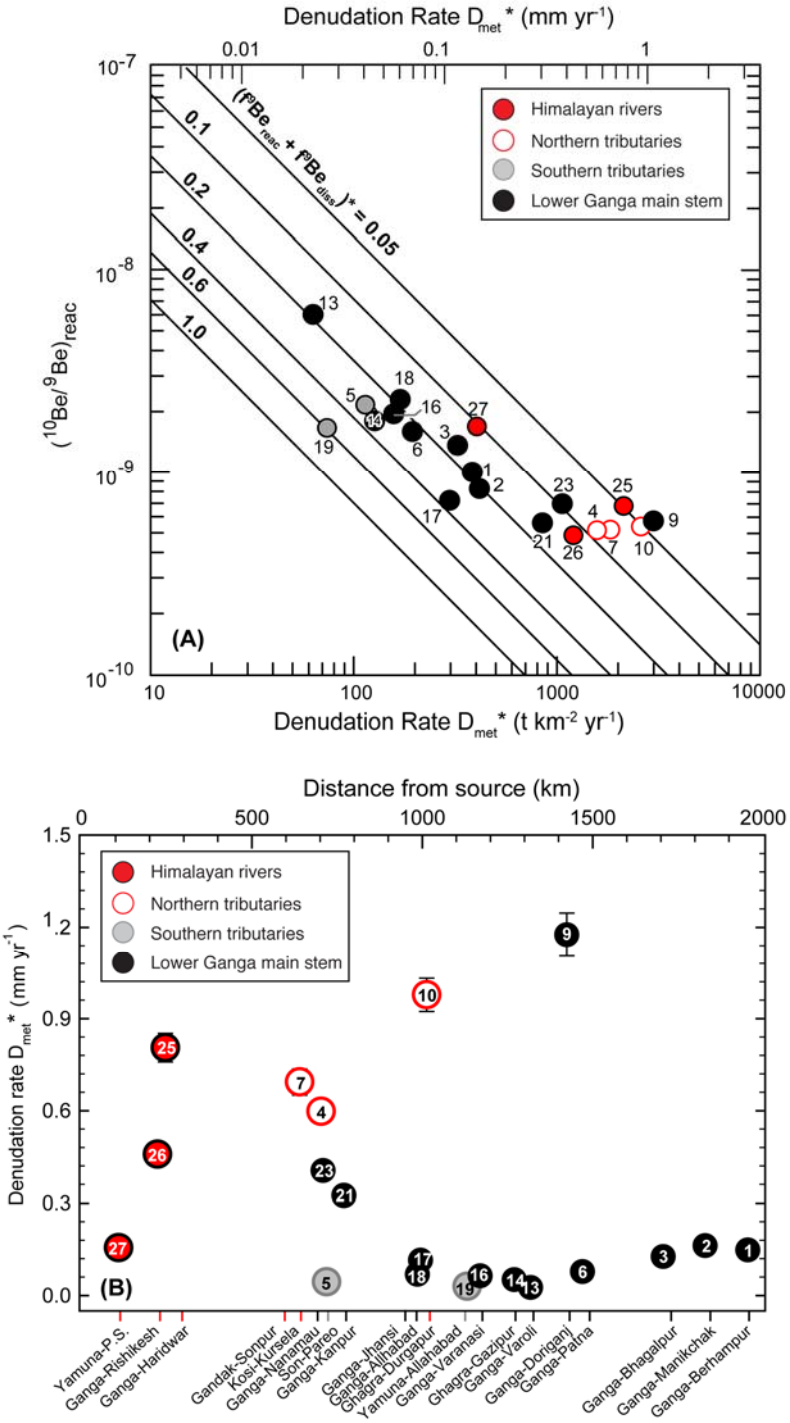

Figure 5) A) $(f_{reac}^{9Be} + f_{diss}^{9Be}) *$ as function of $(^{10}Be/^{9}Be)_{reac}$ versus D_{met}*. The model was calculated using a basin-wide average depositional flux of 1.04×10^{6} at cm^{-2} yr^{-1}. Bold values give $(f_{reac}^{9Be} + f_{diss}^{9Be}) *$ as proxy for weathering; a value of $(f_{reac}^{9Be} + f_{diss}^{9Be}) *$ = 1 would indicate complete weathering. Numbers give GMSS-sample numbers ("P.S." is Yamuna at Ponta Sahib). Lowest $(f_{reac}^{9Be} + f_{diss}^{9Be}) *$ are observed for rivers that drain the Himalayas (red symbols); highest $(f_{reac}^{9Be} + f_{diss}^{9Be}) *$ are observed for southern tributaries (grey symbols). These southern rivers $(f_{reac}^{9Be} + f_{diss}^{9Be}) *$ plotted here differ from their calculated $(f_{reac}^{9Be} + f_{diss}^{9Be}) *$ (Table 4), as F_{met}^{10Be} values for these basins are much lower than the basin-average F_{met}^{10Be} used to construct $(f_{reac}^{9Be} + f_{diss}^{9Be}) *$ model curves. B) Sorting-corrected denudation rate D_{met}* from upstream to downstream (measured along main stem). Note that for GMSS-7, 13 and 17, no sorting correction was applied (Table 1). Most uncertainties in A and B are smaller than symbol sizes (only internal uncertainties, i.e. analytical 5% uncertainties of ^{9}Be and ^{10}Be concentrations and a 0.5 µg g^{-1} uncertainty for $[^{9}Be]_{parent}$ were propagated).

6.3 Variability of basin-wide denudation rates

Meteoric denudation rates D_{met}* decrease from 0.5-0.7 mm yr^{-1} in the Ganga headwaters at Rishikesh and Haridwar to <0.1 mm yr^{-1} in the Ganga lowlands (Fig. 5B, Table 4). Similarly, D_{met}* decrease from 0.15 mm yr^{-1} in the Yamuna headwaters to 0.03 mm yr^{-1} at Allahabad. For the Yamuna this decrease can be attributed to the contribution of slowly eroding cratonic areas. D_{met}* is similar at 0.04 mm yr^{-1} for the Son River, the only tributary measured that drains entirely cratonic areas. Nevertheless, we find virtually no decrease in D_{met}* downstream of these lowland confluences. In contrast, main stem denudation rates increase after confluences with Himalayan tributaries that show high denudation rates (Fig. 5B). We infer from this contrasting behavior that the denudation signal of the main stem is mainly dominated by the Himalayan tributaries. D_{met}* at the final Ganga outflow amounts to 0.14 mm yr^{-1} (Fig. 6B), which corresponds to a sediment flux of 350 Mt yr^{-1} when using the drainage area at this location (93.5×10^4 km^2) for conversion. This integrated D_{met}* thus comprises a mixture of Himalayan D, Indian-craton D, and potentially, albeit weak, modification in the floodplain. We will show in the next section from the comparison with *in situ*-derived denudation rates that this integrated D_{met}* indeed reflects the full catchment-wide denudation rate.

6.4 Comparison of meteoric-derived with *in situ*-derived denudation rates

We can compare our D_{met}* with *in situ*-derived denudation rates (D_{insitu}) from Lupker et al. (2012a) and Scherler et al. (2014). In the headwaters of the basin, meteoric-derived denudation rates agree reasonably with D_{insitu} (Fig. 6), except in the upper Yamuna (GMSS-27). There, we measure a D_{met}* of 0.15 mm yr^{-1}, whereas an area-weighed D_{insitu} is 0.76 mm yr^{-1} (see summary in Wittmann and von Blanckenburg

(2016), original data in Lupker et al. (2012a); Scherler et al. (2014)). For cratonic headwater areas, the agreement is low, but the comparison is hampered by the small numbers of samples. D_{insitu} is 0.007 mm yr^{-1} for the Chambal River (Lupker et al., 2012a) and D_{met}* is 0.04 mm/y for the Son River (Section 6.3). The low D_{insitu} for the Chambal River, however, could be underestimated as this river drains large areas of Deccan Trap basalts that do not contain quartz minerals.

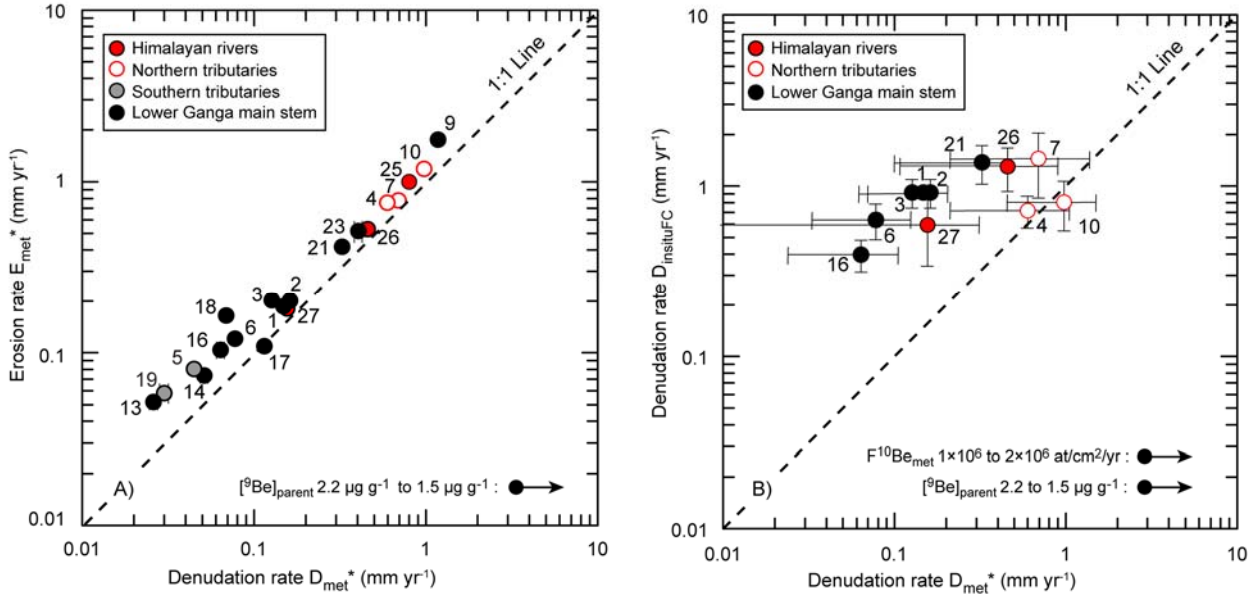

Figure 6) A) Meteoric ^{10}Be-derived erosion rates (E_{met}*, mm yr^{-1}, eq. 1) versus D_{met} * (calculated using $(f_{reac}^{9Be} + f_{diss}^{9Be}) *$ in eq. 2 and a $[^9Be]_{parent}$ of 2.2 µg g^{-1}). Numbers are sample IDs. Arrow indicates the shift if D_{met} would be calculated with a $[^9Be]_{parent}$ of 1.5 µg g^{-1} instead of 2.2 µg g^{-1} in eq. 2. Uncertainties are smaller than symbol size (as a potential bias in the estimate of atmospheric ^{10}Be flux affects both E_{met} and D_{met} to the same extent, only analytical 5% uncertainties of ^{9}Be and ^{10}Be concentrations and a 0.5 µg g^{-1} uncertainty for $[^9Be]_{parent}$ were propagated). B) Meteoric ^{10}Be-derived denudation rates D_{met}* as in 6A) versus floodplain-corrected denudation rates from *in situ* ^{10}Be in river quartz $D_{insituFC}$ (Table 1, Lupker et al. (2012a). For D_{met}*, we propagated analytical uncertainties (a 5% uncertainty for $^9Be_{reac}$ and $^9Be_{min}$, the uncertainty given in Table 3 for the $(^{10}Be/^9Be)_{reac}$ ratio; a 0.5 µg g^{-1} uncertainty for $[^9Be]_{parent}$) and the large external uncertainty for the depositional flux (given in Table 4). The upper arrow shows how D_{met}* would shift if F_{met}^{10Be} were twice as high as the values used. The lower arrow indicates the shift if D_{met}* would be calculated with a $[^9Be]_{parent}$ of 1.5 µg g^{-1} instead of 2.2 µg g^{-1}

In the Ganga lowlands, however, main stem meteoric denudation rates are up to one order of magnitude lower than the floodplain-corrected denudation rates from *in situ* ^{10}Be ($D_{insituFC}$, in mm yr^{-1}, Fig. 6B) from Lupker et al. (2012a). These rates range between 0.8 and 1 mm yr^{-1} in the lower Ganga, which corresponds to a minimum (as D includes the dissolved flux) sediment production flux of ca. 600 Mt yr^{-1} at the Ganga outlet (Lupker et al., 2012a; Wittmann and von Blanckenburg, 2016).

Reconciling our floodplain-D_{met}* with $D_{insituFC}$ (black symbols in Fig. 6B) would be possible if: 1) the meteoric ^{10}Be flux F_{met}^{10Be} in the lowlands relative to the source areas is underestimated by a factor of >4 in eq. 2 (see upper arrow in Fig. 6B). We regard this possibility as unlikely as it is the Himalayan area that is potentially compromised by biased depositional fluxes, and not the lowlands (Supplement S1). 2) the $(f_{reac}^{9Be} + f_{diss}^{9Be}) *$ is underestimated by a factor of >3 in eq. 2. We regard this possibility as unlikely in light of the narrow concentration range of $[^{9}Be]_{reac}$ and $[^{9}Be]_{min}$ (Fig. 2). 3) As mentioned in Section 6.2, an overestimation of $[^{9}Be]_{parent}$ would result in too low D_{met}*. For example, using a $[^{9}Be]_{parent}$ of 1.5 µg g^{-1} instead of 2.2 µg g^{-1} as basin-wide value (Section 3.4) would raise D_{met}* by 47%, as indicated by the lower arrow in Fig. 6B. This calculation would affect all meteoric denudation rates; those in the source areas would then partly exceed those of $D_{insituFC}$ and those in the lowlands would be closer, but would still disagree with $D_{insituFC}$.

Accordingly, we suggest that the remaining differences in denudation rates are mainly due to geological reasons. First, the lithological sources of coarse-grained rock that produces sediment used for D_{insitu} might erode faster than the possibly fine-grained sediment predominantly sampled from suspended loads used for D_{met}*. Therefore, the lower abundance of clay-sized sediment in the Himalayan streams, the main carrier of meteoric ^{10}Be, could account for lower denudation rates whereas

predominantly coarse-grained sediments near the source area provide higher D_{insitu}. Given however the heterogeneous lithologies of the Himalayan headwaters (Fig. 1A), this effect is difficult to discern.

Second, unlike *in situ* ^{10}Be that does not readily accumulate in floodplains due to its low production rate in low elevation floodplains, meteoric ^{10}Be does accumulate in lowlands (Wittmann et al., 2015). At the same time, provided long and deep sediment storage, decay of ^{10}Be may proceed (Wittmann and von Blanckenburg, 2016). In the Ganga basin, however, the similarity between exported sedimentary to depositional fluxes (Fig. 4) provides evidence that neither decay nor accumulation of ^{10}Be during burial or surficial storage, respectively, plays a significant role in modifying $[^{10}Be]_{reac}$ across the Ganga floodplain. This is most likely due to the short (few kyr) storage times encountered in the Ganga floodplain. Assuming, for example, a minimum sediment residence time in the active Ganga floodplain of ca. 1400 yrs (Lupker et al., 2012a), we can estimate that during this time and assuming negligible erosion, ca. 0.75×10^7 at g^{-1} of $[^{10}Be]_{reac}$ should accumulate in a 1 m thick soil profile assuming a lowland-depositional flux of 1.0×10^6 at cm^{-2} yr^{-1} and using a sediment density of 2 g cm^{-3} for converting the resulting ^{10}Be inventory back to a ^{10}Be concentration (for details, see eq. 16 in Wittmann et al., 2015). This means that in relation to the $[^{10}Be]_{reac}$* of the Ganga source area (0.8×10^6 at g^{-1}, mean of GMSS-25 and -26), for example, we should record a ca. 2-fold increase in concentration across the floodplain during this residence time. The fact that we do not observe such an increase for purely lowland reaches without headwater-draining tributaries (e.g. between GMSS-25 to 21) supports overall short residence times. For the entire Ganga floodplain, however, a 2-fold increase is potentially contained in the overall high variability in $[^{10}Be]_{reac}$*, which might be due to tributary admixing (see section

6.1). We conclude that D_{met}* and E_{met}* record basin-wide rates, being the mixed sum of all tributaries producing sediment. Thus the meteoric method records a different denudation than floodplain-corrected $D_{insituFC}$, which quantifies denudation in the source areas only.

7. Conclusions

We demonstrate the potential use of the meteoric cosmogenic $^{10}Be/(stable)^{9}Be$ ratio in measuring denudation rates D, erosion rates E, and estimating the degree of weathering from suspended sediments collected from the Ganga and its tributaries. The most important findings are as follows:

1. Over the entire Ganga basin, the depositional ^{10}Be flux broadly agrees with the exported ^{10}Be attached to sediment and the ^{10}Be flux is thus in steady state. On smaller spatial scales, particularly in the Himalayan source areas, this is not the case, which is likely due to an underestimate of the depositional flux. This means that over the spatial scale of the basin, estimates of depositional fluxes are accurate, sediment production is at steady state with sediment export, and the duration of sediment storage is short relative to the Myr-scale decay time scale of ^{10}Be.
2. Most of the reactive ^{10}Be and ^{9}Be is hosted in the amorphous Fe-Mn phase, and Be contained in the crystalline Fe phase is minute as obtained from sequential extraction. $^{10}Be/^{9}Be$ ratios agree between amorphous and crystalline oxide phases and hence indicate sufficient exchange between these oxide phases. Distribution of ^{10}Be and ^{9}Be in these phases testifies to the rapid turnover of

sediment in the basin and its isotopic equilibration. ^{10}Be loss into the dissolved phase is negligible because pH (>8) is high and thus retentivity is also high.

3. Variations in E from $[^{10}Be]_{reac}$, D from $(^{10}Be/^{9}Be)_{reac}$, and the degree of weathering from $(f_{reac}^{9Be} + f_{diss}^{9Be})$ in source area-draining basins are consistent with weathering kinetics, i.e. they indicate that Himalayan tributaries erode rapidly and rocks are not intensely weathered, and craton-draining rivers erode slowly and weathering intensities are high.
4. We find an overall short (few kyr) sediment residence times in the Ganga floodplain as suggested by other studies, given that an increase in $[^{10}Be]_{reac}$ along the largely-tributary free Ganga reach from Haridwar to Kanpur is not resolvable.
5. Published denudation rates from *in situ*-^{10}Be (D_{insitu}), exceed those from meteoric ^{10}Be (D_{met}) by a factor of 1 to 2 in the Himalayan source areas, and by up to a factor of 4-5 in the lower Ganga main stem. These differences exceed any uncertainty potentially introduced in the assumptions on depositional ^{10}Be flux and bedrock ^{9}Be concentration. Thus, in the source areas differences are likely due sampling of sediment from different lithologies eroding at different rates. At the basin outlet, D from meteoric ^{10}Be most likely represents a mixed signal of all tributaries and floodplain processes, whereas floodplain-corrected denudation rates from *in situ*-^{10}Be ($D_{insituFC}$) record the production of sediment in the source area. Unlike its sister nuclide *in situ* ^{10}Be, meteoric ^{10}Be derived D thus records a basin-wide denudation rate.

Acknowledgements

W. Rahaman thanks the Alexander von Humboldt foundation, Germany, for a postdoctoral fellowship. Authors thank the Helmholtz Laboratory for the Geochemistry of the Earth Surface for laboratory infrastructure, and C. Schulz and J. Bartel for laboratory support and help with measuring trace and major elements using ICP-OES, and C. Andermann and S. Liening for performing grain size analysis in GFZ´s "*SedLab*". We are grateful to S. Heinze and S. Binnie from Cologne University for performing AMS measurements. We thank P.J. Frings for suggestions and comments on an earlier version of this manuscript. We thank M. Lupker as well as two anonymous reviewers for constructive comments that significantly improved this manuscript.

Supplement

Supplement Text S1: Assessment of meteoric depositional fluxes

Large-scale meteoric deposition rates (Table 4 of main text) are derived from a combination of a model for the simulation of cosmic ray particle interactions with the Earth's atmosphere (Masarik and Beer, 1999) with the "ECHAM5" fifth-generation global atmospheric circulation model (GCM) coupled to the aerosol model HAM (Heikkilä et al., 2013a; Heikkilä et al., 2013b). This model was run separately for the modern ("industrial") ^{10}Be deposition (Heikkilä et al., 2013a) and for the early Holocene ("pre-industrial") (Heikkilä et al., 2013b) and then combined (see Heikkilä and von Blanckenburg (2015)). Details of the global tabulated meteoric fluxes are available in an online data repository, http://pmd.gfz-potsdam.de/panmetaworks/showshort.php?id=escidoc:977921), with the difference between model runs used as external uncertainty (i.e. used when our results are compared to other methods; see Table 4 of main text). From this combined model, the average area-weighed global flux is 1.09×10^6 at cm^{-2} yr^{-1}. The Himalayan area shows the largest divergence between the modern and the early Holocene model runs (see map 4 in Heikkilä and von Blanckenburg (2015), with absolute differences in flux of locally 1×10^6 at cm^{-2} yr^{-1}). For the Ganga basin, the average meteoric flux is 1.04×10^6 at cm^{-2} yr^{-1} that is used to calculate the model in Figure 5A in the main text.

Supplement S2: Comparison of sorting- versus non-sorting corrected E and D

To assess the effect of our sorting correction (section 3.4, eqs (6) and (7) we have plotted E_{met}* and D_{met}* corrected for sorting against E_{met} and D_{met} uncorrected for sorting. Because the sorting correction results in lower reactive ^{10}Be concentrations

and also changes in $(f_{reac}^{9Be} + f_{diss}^{9Be})$, corrected E_{met} and D_{met} exceed uncorrected rates.

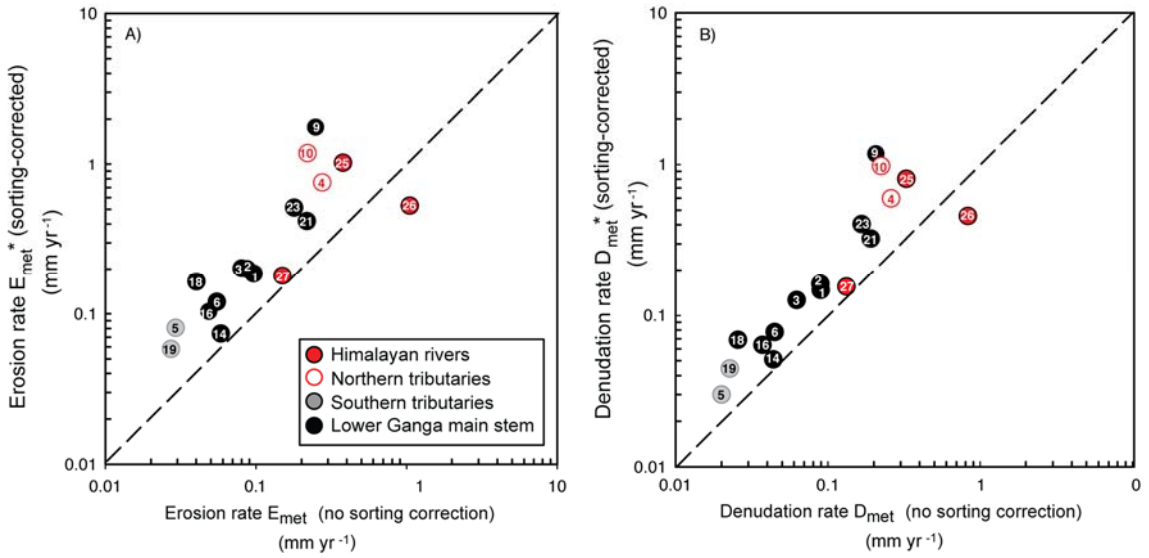

Figure S1) A) Meteoric ^{10}Be-derived erosion rates, E_{met} (mm yr^{-1}) (uncorrected for sorting) versus E_{met} * (mm yr^{-1}) (sorting-corrected). B) Meteoric ^{10}Be-derived denudation rates (mm yr^{-1}), corrected for sorting (D_{met}*) versus uncorrected for sorting (D_{met}). Numbers are sample IDs. Uncertainties are smaller than symbol size. We propagated analytical uncertainties (a 5% uncertainty for $^{9}Be_{reac}$ and $^{9}Be_{min}$, the uncertainty given in Table 3 of the main text for the $(^{10}Be/^{9}Be)_{reac}$ ratio; a 0.5 µg g^{-1} uncertainty for $[^{9}Be]_{parent}$). As we compare within the same method here, we have not propagated the large external uncertainty of the depositional flux. Note that as a grain size correction was not carried out for samples GMSS-7, 13 and 17, we excluded these samples from this plot.

References

Bagard, M.-L., West, A.J., Newman, K., Basu, A.R., 2015. Lithium isotope fractionation in the Ganges–Brahmaputra floodplain and implications for groundwater impact on seawater isotopic composition. Earth and Planetary Science Letters 432, 404-414.

Blott, S.J., Pye, K., 2001. GRADISTAT: a grain size distribution and statistics package for the analysis of unconsolidated sediments. Earth Surface Processes and Landforms 26, 1237-1248.

Bouchez, J., Lupker, M., Gaillardet, J., France-Lanord, C., Maurice, L., 2011. How important is it to integrate riverine suspended sediment chemical composition with depth? Clues from Amazon River depth-profiles. Geochimica Et Cosmochimica Acta 75, 6955-6970.

Burbank, D.W., Blythe, A.E., Putkonen, J., Pratt-Sitaula, B., Gabet, E., Oskin, M., Barros, A., Ojha, T.P., 2003. Decoupling of erosion and precipitation in the Himalayas. Nature 426, 652-655.

Chmeleff, J., von Blanckenburg, F., Kossert, K., Jakob, D., 2010. Determination of the ^{10}Be half-life by multicollector ICP-MS and liquid scintillation counting. Nuclear Instruments & Methods in Physics Research Section B- Beam Interactions with Materials and Atoms 268, 192-199.

Dewald, A., Heinze, S., Jolie, J., Zilges, A., Dunai, T., Rethemeyer, J., Melles, M., Staubwasser, M., Kuczewski, B., Richter, J., Radtke, U., von Blanckenburg, F., Klein, M., 2013. CologneAMS, a dedicated center for accelerator mass spectrometry in Germany. Nuclear Instruments and Methods in Physics Research Section B: Beam Interactions with Materials and Atoms 294, 18-23.

Foster, M.A., Anderson, R.S., Wyshnytzky, C.E., Ouimet, W.B., Dethier, D.P., 2015. Hillslope lowering rates and mobile-regolith residence times from in situ and meteoric 10Be analysis, Boulder Creek Critical Zone Observatory, Colorado. Geological Society of America Bulletin 127, 862-878.

France-Lanord, C., Derry, L., Michard, A., 1993. Evolution of the Himalaya since Miocene time: isotopic and sedimentological evidence from the Bengal Fan. Geological Society, London, Special Publications 74, 603-621.

Frings, P.J., Clymans, W., Fontorbe, G., Gray, W., Chakrapani, G., Conley, D.J., De La Rocha, C., 2015. Silicate weathering in the Ganges alluvial plain. Earth and Planetary Science Letters 427, 136-148.

Gabet, E.J., Burbank, D.W., Pratt-Sitaula, B., Putkonen, J., Bookhagen, B., 2008. Modern erosion rates in the High Himalayas of Nepal. Earth and Planetary Science Letters 267, 482-494.

Galy, A., France-Lanord, C., 2001. Higher erosion rates in the Himalaya: Geochemical constraints on riverine fluxes. Geology 29, 23-26.

Galy, V., France-Lanord, C., Beyssac, O., Faure, P., Kudrass, H., Palhol, F., 2007. Efficient organic carbon burial in the Bengal fan sustained by the Himalayan erosional system. Nature 450, 407-U406.

Heikkilä, U., Beer, J., Abreu, J.A., Steinhilber, F., 2013a. On the Atmospheric Transport and Deposition of the Cosmogenic Radionuclides (10Be): A Review. Space Science Reviews 176, 321-332.

Heikkilä, U., Phipps, S.J., Smith, A.M., 2013b. Be-10 in late deglacial climate simulated by ECHAM5-HAM - Part 1: Climatological influences on Be-10 deposition. Climate of the Past 9, 2641-2649.

Heikkilä, U., von Blanckenburg, F., 2015. The global distribution of Holocene meteoric 10Be fluxes from atmospheric models. Distribution maps for terrestrial Earths surface applications. GFZ Data Services, GFZ Potsdam.

Herman, F., Copeland, P., Avouac, J.-P., Bollinger, L., Mahéo, G., Le Fort, P., Rai, S., Foster, D., Pêcher, A., Stüwe, K., Henry, P., 2010. Exhumation, crustal deformation, and thermal structure of the Nepal Himalaya derived from the inversion of thermochronological and thermobarometric data and modeling of the topography. Journal of Geophysical Research: Solid Earth 115, B06407.

Kısakűrek, B., James, R.H., Harris, N.B.W., 2005. Li and δ7Li in Himalayan rivers: Proxies for silicate weathering? Earth and Planetary Science Letters 237, 387-401.

Korschinek, G., Bergmaier, A., Faestermann, T., Gerstmann, U.C., Knie, K., Rugel, G., Wallner, A., Dillmann, I., Dollinger, G., von Gostomski, C.L., Kossert, K., Maiti, M., Poutivtsev, M., Remmert, A., 2010. A new value for the half-life of ^{10}Be by heavy-ion elastic recoil detection and liquid scintillation counting. Nuclear Instruments & Methods in Physics Research Section B- Beam Interactions with Materials and Atoms 268, 187-191.

Lavé, J., Avouac, J.P., 2001. Fluvial incision and tectonic uplift across the Himalayas of central Nepal. Journal of Geophysical Research: Solid Earth 106, 26561-26591.

Lupker, M., Blard, P.-H., Lavé, J., France-Lanord, C., Leanni, L., Puchol, N., Charreau, J., Bourlès, D., 2012a. ^{10}Be-derived Himalayan denudation rates and sediment budgets in the Ganga basin. Earth and Planetary Science Letters 333-334, 146-156.

Lupker, M., France-Lanord, C., Galy, V., Lavé, J., Gaillardet, J., Gajurel, A.P., Guilmette, C., Rahman, M., Singh, S.K., Sinha, R., 2012b. Predominant floodplain over mountain weathering of Himalayan sediments (Ganga basin). Geochimica Et Cosmochimica Acta 84, 410-432.

Lupker, M., France□Lanord, C., Lave, J., Bouchez, J., Galy, V., Métivier, F., Gaillardet, J., Lartiges, B., Mugnier, J.L., 2011. A Rouse□based method to integrate the chemical composition of river sediments: Application to the Ganga basin. Journal of Geophysical Research: Earth Surface (2003–2012) 116.

Maher, K., von Blanckenburg, F., 2016. Surface ages and weathering rates from ^{10}Be(meteoric) and ^{10}Be/^{9}Be: insights from differential mass balance and reactive transport modeling. Chemical Geology 446, 70-86.

Métivier, F., Gaudemer, Y., 1999. Stability of output fluxes of large rivers in South and East Asia during the last 2 million years: implications on floodplain processes. Basin Research 11, 293-303.

Rahaman, W., Singh, S.K., Sinha, R., Tandon, S.K., 2009. Climate control on erosion distribution over the Himalaya during the past ~100 ka. Geology 37, 559-562.

Rahaman, W., Singh, S.K., Sinha, R., Tandon, S.K., 2011. Sr, C and O isotopes in carbonate nodules from the Ganga Plain: Evidence for recent abrupt rise in dissolved 87Sr/86Sr ratios of the Ganga. Chemical Geology 285, 184-193.

Rai, S.K., Singh, S.K., Krishnaswami, S., 2010. Chemical weathering in the Plain and Peninsular sub-basins of the Ganga: Impact on Major ion chemistry and Elemental Fluxes. Geochimica Et Cosmochimica Acta 74, 2340-2355.

Rudnick, R.L., Gao, S., 2004. Composition of the Continental Crust, in: Heinrich, D.H., Karl, K.T. (Eds.), Treatise on Geochemistry. Elsevier, Amsterdam, pp. 1-64.

Sarin, M.M., Krishnaswami, S., Dilli, K., Somayajulu, B.L.K., Moore, W.S., 1989. Major ion chemistry of the Ganga-Brahmaputra river system: Weathering processes and fluxes to the Bay of Bengal. Geochimica et Cosmochimica Acta 53, 997-1009.

Sarkar, S., Roy, A.K., Martha, T.R., 2013. Soil depth estimation through soil-landscape modelling using regression kriging in a Himalayan terrain. International Journal of Geographical Information Science 27, 2436-2454.

Scherler, D., Bookhagen, B., Strecker, M.R., 2014. Tectonic control on 10Be-derived erosion rates in the Garhwal Himalaya, India. Journal of Geophysical Research: Earth Surface 119, 1-23.

Shen, C., Beer, J., Kubik, P.W., Suter, M., Borkovec, M., Liu, T.S., 2004. Grain size distribution, ^{10}Be content and magnetic susceptibility of micrometer-nanometer loess materials. Nuclear Instruments and Methods in Physics Research Section B: Beam Interactions with Materials and Atoms 223-224, 613-617.
Singh, M., Singh, I.B., Müller, G., 2007. Sediment characteristics and transportation dynamics of the Ganga River. Geomorphology 86, 144-175.
Singleton, A.A., Schmidt, A.H., Bierman, P.R., Rood, D.H., Neilson, T.B., Greene, E.S., Bower, J.A., Perdrial, N., 2017. Effects of grain size, mineralogy, and acid-extractable grain coatings on the distribution of the fallout radionuclides 7Be, 10Be, 137Cs, and 210Pb in river sediment. Geochimica et Cosmochimica Acta 197, 71-86.
Thiede, R.C., Ehlers, T.A., Bookhagen, B., Strecker, M.R., 2009. Erosional variability along the northwest Himalaya. Journal of Geophysical Research-Earth Surface 114.
Tripathy, G.R., Singh, S.K., 2010. Chemical erosion rates of river basins of the Ganga system in the Himalaya: Reanalysis based on inversion of dissolved major ions, Sr, and 87Sr/86Sr. Geochemistry, Geophysics, Geosystems 11, n/a-n/a.
Vance, D., Bickle, M., IvyOchs, S., Kubik, P., 2003. Erosion and exhumation in the Himalaya from cosmogenic isotope inventories of river sediments. Earth and Planetary Science Letters 206, 273-288.
von Blanckenburg, F., Bouchez, J., Wittmann, H., 2012. Earth surface erosion and weathering from the ^{10}Be (meteoric)/^{9}Be ratio. Earth and Planetary Science Letters 351-352, 295-305.
Willenbring, J.K., von Blanckenburg, F., 2010. Meteoric cosmogenic Beryllium-10 adsorbed to river sediment and soil: Applications for Earth-surface dynamics. Earth-Science Reviews 98, 105-122.
Wittmann, H., von Blanckenburg, F., 2016. The geological significance of cosmogenic nuclides in large lowland river basins. Earth Science Reviews 159, 118-141.
Wittmann, H., von Blanckenburg, F., Bouchez, J., Dannhaus, N., Naumann, R., Christl, M., Gaillardet, J., 2012. The dependence of meteoric ^{10}Be concentrations on particle size in Amazon River bed sediment and the extraction of reactive ^{10}Be/^{9}Be ratios. Chemical Geology 318-319, 126-138.
Wittmann, H., von Blanckenburg, F., Dannhaus, N., Bouchez, J., Gaillardet, J., Guyot, J.L., Maurice, L., Roig, H., Filizola, N., Christl, M., 2015. A test of the cosmogenic ^{10}Be(meteoric)/^{9}Be proxy for simultaneously determining basin-wide erosion rates, denudation rates, and the degree of weathering in the Amazon basin. Journal of Geophysical Research: Earth Surface, 120, 2498-2528.
Wittmann, H., von Blanckenburg, F., Maurice, L., Guyot, J.L., Filizola, N., Kubik, P.W., 2011. Sediment production and delivery in the Amazon River basin quantified by in situ-produced cosmogenic nuclides and recent river loads. Geological Society of America Bulletin 123, 934-950.